Brookhaven National Laboratory

BNL-225119-2023-JAAM

Toward Low-Thermal-Budget Hafnia-Based Ferroelectrics via Atomic Layer Deposition

J. Kim, Y. Zhang

To be published in "ACS Applied Electronic Materials"

September 2023

Center for Functional Nanomaterials

Brookhaven National Laboratory

U.S. Department of Energy

USDOE Office of Science (SC), Basic Energy Sciences (BES). Scientific User Facilities (SUF)

Notice: This manuscript has been authored by employees of Brookhaven Science Associates, LLC under Contract No.DE-SC0012704 with the U.S. Department of Energy. The publisher by accepting the manuscript for publication acknowledges that the United States Government retains a non-exclusive, paid-up, irrevocable, world-wide license to publish or reproduce the published form of this manuscript, or allow others to do so, for United States Government purposes.

DISCLAIMER

This report was prepared as an account of work sponsored by an agency of the United States Government. Neither the United States Government nor any agency thereof, nor any of their employees, nor any of their contractors, subcontractors, or their employees, makes any warranty, express or implied, or assumes any legal liability or responsibility for the accuracy, completeness, or any third party's use or the results of such use of any information, apparatus, product, or process disclosed, or represents that its use would not infringe privately owned rights. Reference herein to any specific commercial product, process, or service by trade name, trademark, manufacturer, or otherwise, does not necessarily constitute or imply its endorsement, recommendation, or favoring by the United States Government or any agency thereof or its contractors or subcontractors. The views and opinions of authors expressed herein do not necessarily state or reflect those of the United States Government or any agency thereof.

Towards Low-thermal-budget Hafnia-based Ferroelectrics via Atomic Layer Deposition

*Jin-Hyun Kim[1], Takashi Onaya[2, 3], Hye Ryeon Park[4], Yong Chan Jung[1], Dan N. Le[1], Minjong Lee[5], Heber Hernandez-Arriaga[1], Yugang Zhang[6], Esther H. R. Tsai[6], Chang-Yong Nam[6, 7], Toshihide Nabatame[3], Si Joon Kim[4, 8, *] and Jiyoung Kim[1, 5 *]*

[1] Department of Materials Science and Engineering, The University of Texas at Dallas, 800 West Campbell Road, Richardson, Texas 75080, USA

[2] Department of Advanced Materials Science, Graduate School of Frontier Science, The University of Tokyo, 5-1-5 Kashiwanoha, Kashiwa-shi, Chiba 277-8561, Japan

[3] National Institute for Materials Science (NIMS), 1-1 Namiki, Tsukuba, Ibaraki 305-0044, Japan

[4] Department of BIT Medical Convergence, Kangwon National University, 1 Gangwondaehakgil, Chuncheon, Gangwon-do 24341, Republic of Korea

[5] Department of Electrical and Computer Engineering, The University of Texas at Dallas, 800 West Campbell Road, Richardson, Texas 75080, USA

[6] Center for Functional Nanomaterials, Brookhaven National Laboratory, Upton, New York 11973, United States

[7] Department of Materials Science and Chemical Engineering, Stony Brook University, Stony Brook, New York 11794, United States

[8] Department of Electrical and Electronics Engineering, Kangwon National University, 1

Gangwondaehakgil, Chuncheon, Gangwon-do 24341, Republic of Korea

KEYWORDS

Hafnia, Ferroelectric, Low-temperature, Back-end-of-line, Atomic layer deposition

ABSTRACT

Since the first report of ferroelectricity in fluorite structure oxides a decade ago, significant attention has been devoted to studying hafnia-based ferroelectric material systems due to their promising properties and opportunities. To achieve such ferroelectric fluorite structure oxides at low temperatures (below 400 °C), stabilizing the metastable non-centrosymmetric orthorhombic phase is crucial. This review provides a comprehensive overview of atomic layer deposition (ALD) techniques for obtaining the orthorhombic phase for low-temperature ferroelectric applications. We discuss optimization of ALD process for synthesizing high-quality, low-temperature crystallizing ferroelectric films, including doping, precursor and oxygen source selection, deposition temperature, and interface engineering. In addition, the techniques for stabilizing the ferroelectric phase by regulating the thermal budget and stress with various annealing methods and stressors are discussed. The review focuses on different techniques to reduce the thermal budget required to acquire ferroelectricity, making hafnia-based ferroelectric materials compatible with back-end-of-line and three-dimensional integration for a variety of future applications, including flexible electronics applications.

1. INTRODUCTION

Hafnium oxide (HfO_2) is a widely used high-k dielectric material replacing silicon oxide owing to its high dielectric constant and wide bandgap. While continuing on the improvement of the dielectric constant, Böscke et al. were the first to discover the ferroelectricity of HfO_2 in 2011.[1] The discovery of ferroelectric HfO_2 has revolutionized ferroelectric technology because of its compatibility with complementary metal-oxide-semiconductor (CMOS) technology as well as scalability. After that, significant efforts have been devoted to understand the underlying physical mechanisms. Both theoretical and experimental studies have found that the ferroelectric properties of HfO_2 are attributable to the noncentrosymmetric orthorhombic phase (o-phase, space group: $Pca2_1$).[1–4] As shown by additional research, controlling the film thickness, grain size, doping, interface, and vacancy, among other factors, can stabilize the o-phase.[1,5–8] Over the years, the development of HfO_2-base materials has facilitated a vast array of innovative research and applications for energy storage and harvesting, low-energy neuromorphic computing, and logic and memory devices to name a few.[9] In particular, ferroelectric HfO_2-based non-volatile memories such as ferroelectric tunnel junction (FTJ), ferroelectric field effect transistor (FeFET), and ferroelectric random access memory (FRAM), exhibited great potential by providing faster writing speeds, longer lifetimes, and lower power consumption than charge trap-based flash memory applications.[10–13]

As electronic devices continue to downscale, the limitations of conventional perovskite-based FRAM (e.g., lead zirconium titanate (PZT), barium titanate ($BaTiO_3$)) have become more apparent, such as high leakage current under 50 nm. In contrast, HfO_2-based ferroelectrics have demonstrated robust ferroelectricity and minimum leakage current even when scaled below 10 nm, thanks to their wide bandgap (>5.1 eV).[14–18] To achieve nanometer-scale film thickness

required for such HfO_2-based devices, vapor-phase deposition techniques, like atomic layer deposition (ALD), is the conventional technique used in the industry. The deposition method offers distinct advantages over physical vapor deposition (PVD) and chemical solution deposition (CSD) processes in terms of precise control of film thickness at the atomic level, exceptional step coverage over complex features, and the ability to produce highly uniform and conformal thin films across the entire wafer.[19] Besides difficulties in thickness scaling, PVD and CSD tend to deliver crystalline HfO_2-based thin films that exhibit paraelectric monoclinic phase (m-phase),[7,20] which is generally unsuitable for back-end-of-line (BEOL) process because of the need for a subsequent high-temperature annealing step to transform the m- to tetragonal- (t-) or o-phase.[18] Although the deposition parameters of PVD and CSD could be controlled to fit BEOL-compatible temperatures, it is still challenging to achieve robust ferroelectric properties that are comparable to those of ALD HfO_2-based thin films at the same thermal budget.[21] This makes ALD HfO_2-based ferroelectrics an ideal material for high-density three-dimensional (3D) memory applications since they exhibit better electrical properties in comparison to Pb-perovskite-based materials at nanometer scale and is BEOL-compatible.[22]

In addition to scalability and 3D compatibility, ALD HfO_2-based materials offer another advantage in terms of low thermal budget. This means that the ferroelectricity of HfO_2-based materials, particularly when HfO_2 is alloyed with zirconium oxide (ZrO_2), can be achieved at temperatures below 400 °C—i.e., below the upper limit that an underlying CMOS device layer can withstand—by carefully controlling the ALD process and annealing parameters. Such low-temperature ferroelectric was made possible by the fact that these oxides share the same crystal structure, allowing them to form a complete solid solution.[18,23] The solid solution formation between ZrO_2 and HfO_2 results in a lower crystallization temperature than pure HfO_2, enabling

lower o-phase crystallization temperature, while allowing for a controlled transition from ferroelectric to antiferroelectric characteristics by controlling the Hf and Zr composition.[9,10,18,20] Owing to such facile control of properties and the availability of precursors for HfO_2 and ZrO_2 ALD, $Hf_xZr_{1-x}O_2$ systems, particularly $Hf_{0.5}Zr_{0.5}O_2$ (HZO) with robust ferroelectric properties, have been the most extensively studied HfO_2-based ferroelectrics. To demonstrate the strategies for low-temperature ferroelectric applications, this review concentrates on the HfO_2-ZrO_2 solid solution system, particularly HZO systems deposited via ALD.

Besides dopant, numerous additional factors (e.g., metal precursors, oxidation sources, ALD temperature, stressors, etc.) can influence the thermal budget to lower the crystallization temperature of ferroelectric o-phase of ALD Hf-based materials below 400 °C,[10,22] as shown in Figure 1. A typical ferroelectric capacitor fabrication process for characterizing ferroelectric properties involves depositing a sandwiched HZO structure between the top and bottom electrodes on an insulating or semiconducting substrate. Extensive research has also demonstrated the crucial role of top and bottom electrode stressors in achieving robust ferroelectric properties with a limited thermal budget. Since the ferroelectric o-phase is a metastable phase at low temperatures and atmospheric pressure environment, applying stress to stabilize the o-phase is necessary. Without these stressors, the HZO film will crystallize to a more thermodynamically stable paraelectric monoclinic phase (m-phase).[10,22,24] The stronger stress generated by the top and bottom electrodes sandwiching the HZO layer results in a higher stabilization o-phase, enabling a higher o/m-phase ratio with the same thermal budget and potentially lowering the process temperature. Furthermore, the crystallization temperature of HZO and formation of o-phase also depend on thermal annealing time and the annealing environment (e.g., chamber pressure, etc.).[25,26] These process variables enable the integration of

low-temperature ferroelectrics with BEOL processes across a broad range of applications such as FRAM, FTJ, and metal-ferroelectric-metal-insulator-semiconductor-based (1T1C) FeFET, resulting in larger effective areas without changing the front-end-of-line configuration.[11,13,27] Overall, by combining these methods with others that will be introduced, it is possible to not only achieve BEOL compatibility but also reduce the process temperature and make the technology suitable for monolithic 3D integration and flexible electronic applications.

Herein, we report a comprehensive review of process strategies to achieve HZO ferroelectric thin films based on ALD techniques. The strategies focus on process variables that enable the reproducible and dominant delivery of the metastable ferroelectric o-phase while reducing the thermal budget. The report discusses the factors that affect the process, including doping, precursor and oxidant selection, plasma effect, interface modification, stress control, and different annealing methods, all of which can impact the thermal budget.[10,18,22,28] Each factor will be discussed and categorized into two major strategies for achieving lower thermal budget ferroelectrics: improving film quality through densification to crystallize at lower temperatures and strain control to promote o-phase formation and maximize the o-phase ratio with a limited thermal budget. The reasoning behind the low-temperature crystallization of HZO will also be discussed. This comprehensive review is expected to provide new insights and reasonings for a better understanding of low-temperature ferroelectrics.

Figure 1.

2. ATOMIC LAYER DEPOSITION

As previously discussed, PVD (e.g., sputter, pulsed laser deposition (PLD), etc.), CSD, and ALD are various techniques that can be employed to achieve ferroelectrics HfO_2-based materials.

However, with the downscaling of devices and the need for BEOL compatibility, ALD has been shown to be the most suitable approach, as it allows for the formation of dense amorphous HZO thin films, depending on the selection of metal precursors and oxidant sources. Such dense amorphous phases, with appropriate local order, can be readily transformed to o-phase by low-temperature annealing processing (< 400 °C). [18,29,30] In contrast, PVD-based and CSD-based thin films do not exhibit similar characteristics to ALD-based HZO (e.g., chemically homogeneous, short-range ordered metal and oxygen atoms, etc.), and therefore, phase transformation at BEOL compatible temperature cannot occur easily.[31]

During a typical ALD process of HZO, Hf-precursor molecules are adsorbed onto the substrate surface in a self-limiting manner, followed by their reaction with subsequent oxidant. Zr-precursor is then introduced into the reactant chamber and reacts with the available reactive sites. Afterward, an oxidant exposure step is followed. This sequential process generates new reaction sites for further ALD cycles, enabling precise control over the thickness and composition of HZO thin films. However, for these surface reactions to occur efficiently, a specific range of temperatures, also known as the ALD window, is required. Deposition at temperatures below the minimum of the ALD window can lead to poor surface reactivity or precursor condensation, while deposition at temperatures above the ALD window can result in precursor decomposition or desorption from the surface. For example, in order to deposit HfO_2 thin film using ALD, Hf precursor, and oxygen sources that are stable and compatible with the targeted ALD temperature range need to be carefully chosen. Additionally, specific Hf precursors with different ligands can be chosen depending on the desired growth rate and to avoid contamination, as the surface reaction depends on the precursor's chemical properties, such as steric hindrance and reactivity.[32,33] Likewise, different oxygen sources may be selected to

deliver desired growth rates, densities, and more, utilizing various reaction mechanisms such as ligand exchange reaction of water (H_2O) and combustion reaction of ozone (O_3) and oxygen (O_2) plasma.[18,31,34,35] Thus, selecting appropriate precursors and oxidants to achieve desirable film properties is critical in ALD.

This section will explore recently reported process variables (e.g., dopants, metal precursors, oxidant sources, etc.) of ALD HZO that can be adjusted to achieve a low thermal budget ferroelectric o-phase. Table 1 provides detailed information about these process variables and their impact on ferroelectric characteristics such as remnant polarization (P_r), coercive field (E_c), and endurance, as reported in recent literature. Section 2.1 will provide a brief overview of the effects of dopants, other than Zr, in HfO_2-based ferroelectrics, while sections 2.2 and 2.3 will cover the selection of metal precursors and oxidants, respectively.

Table 1.

2.1 Dopant selection

Achieving ferroelectric properties in pure HfO_2 can be accomplished by optimizing deposition temperature and oxidant dose, according to recent studies.[36–39] Materano et al. found that insufficient oxygen can promote the formation of the ferroelectric o-phase, which was corroborated by Pal et al.[37,38] In addition, Kim et al. and Polakowshi et al. demonstrated that grain size could be controlled to achieve ferroelectric HfO_2 by varying the deposition temperature and thickness, with the smaller grain size exhibiting a higher o-phase ratio and P_r.[36,39] However, small P_r and high annealing temperature requirements limit the use of pure HfO_2 as a low thermal budget ferroelectric material, and the need to reduce the process temperature necessitated the addition of dopants to aid in the formation of ferroelectric o-phase.

With additional dopants, the overall crystallization temperature of HZO can be controlled. Batra et al. proposed that the lattice distortion caused by dopants can reduce the free energy of the o-phase, making its formation easier due to smaller energy differences with the stable m-phase. In addition, Batra et al. demonstrated first-principle calculations of 40 dopants to select dopants that can assist in stabilizing the polar phase of HfO_2.[40] These dopants can be incorporated into HfO_2 using metal-organic precursors for ALD. As previously mentioned, during the deposition of HfO_2 via ALD, the dopant precursors can be introduced as a full cycle with precursor and oxidant exposure between the HfO_2 deposition cycles. The amount of dopant can be controlled by changing the number of dopant cycles inserted into the HfO_2 deposition cycles, resulting in a supercycle, which is a repeating cycle of HfO_2 and dopants cycles.[34] Numerous researchers have employed this ALD doping technique to achieve ferroelectricity in HfO_2 using various dopants, including Al,[41,42] Si,[42–44] Y,[45] La,[42,46] Sr,[47,48] Gd,[47] and Zr[25,29,38,49–70]. Doping HfO_2 with Gd, Sr, La, Y, and Zr showed an improvement in $2P_r$ values compared to pure HfO_2, as demonstrated in Figure 2a, satisfying the minimum switching charge density requirement (24.0 $\mu C/cm^2$) for FRAM applications according to International Roadmap for Devices and Systems.[71] Moreover, the presence of Gd and Zr as dopants in HfO_2 also helped achieve ferroelectricity at temperatures compatible with the BEOL process (< 450 °C). Overall, Zr doping showed the lowest processing temperature (< 400 °C) to obtain ferroelectricity compared to other dopants, making Zr-doped HfO_2 an ideal material for low-temperature ferroelectric applications. These low-temperature ferroelectric properties by doping Zr originated from the relatively low-temperature crystallization temperature of ALD ZrO_2 compared to other oxide materials.[9,72] As previously stated, ZrO_2 and HfO_2 can form a solid solution for a wide range of concentrations, with higher Zr concentration leading to lower crystallization

temperature.[18,23,72] Furthermore, the t-phase present in ALD ZrO_2 helps suppress the formation of the m-phase in HfO_2 while also stabilizing the ferroelectric o-phase by lowering the free energy.[3] Kim et al. and Oh et al. showed the evolution of ferroelectric properties of HZO by changing the Zr content with thermal ALD (TALD) at BEOL compatible temperature.[9,61] The results indicated that pure HfO_2 remained amorphous state after annealing due to the high crystallization temperature, exhibiting paraelectric properties. By introducing higher levels of Zr doping, the film crystallized at a temperature compatible with BEOL requirements and exhibited ferroelectric properties. Notably, the maximum polarization was achieved at a Zr atomic ratio of 0.5. Further Zr doping led to the emergence of antiferroelectric characteristics. Moreover, Hsain et al. conducted a study on phase evolution and crystallization temperature in relation to the HfO_2-ZrO_2 ratio using high-temperature in-situ X-ray diffraction.[72] According to their findings, pure HfO_2 exhibited crystallization around 386 °C. However, as the proportion of ZrO_2 increased, the crystallization temperature decreased to 300 °C. Interestingly, in films with a higher HfO_2 ratio, crystallization took place to the m-phase. However, as the ZrO_2 content increased, the proportion of the m-phase diminished, giving rise to the development of t- and o-phases which is favorable for achieving improved ferroelectric properties. This demonstrates the impact of ZrO_2 in reducing the crystallization temperature of HZO films. Furthermore, the substantial solubility and wide concentration range of ZrO_2 in HfO_2 to have ferroelectricity allow easier uniformity control of ferroelectric properties across the wafer.[22] These advantages facilitate the adoption of ferroelectric HZO in industry and BEOL applications, making HZO one of the most intensively researched ferroelectric material systems.[10]

2.2 Precursor selection

ALD films utilize metal precursors that are metal elements converted into vapor phases by introducing inorganic (e.g., halides, etc.) and organic ligands (e.g., hydrocarbon, amine, etc.). Because each ligand has a unique chemical composition, bond strength between metals, and physical shape, each metal precursor has distinct properties that can be utilized for a variety of ALD process requirements. Thus, the properties of the precursors must be considered to fit the ALD system configuration and desired process parameters, such as deposition temperature, pressure, growth rate, reactivity with the oxidant source, contamination from precursor ligands, and more.[34] Therefore, for low-temperature applications, precursors with ALD windows around BEOL-compatible temperatures must be utilized for self-limiting ALD reactions, as opposed to condensation or no reaction. As shown in Table 1, a variety of precursors, such as hafnium tetrachloride ($HfCl_4$),[36,47,48,62,63] tetrakis(ethylmethylamido)hafnium (TEMA-Hf),[38,39,41,42,44–46,54–58,64] tetrakis(dimethylamido)hafnium (TDMA-Hf),[25,29,37,43,49–53,64–69] cyclopentadienyltris(dimethylamino)hafnium (CpHf),[59–61] and more, were used to deposit ferroelectric HfO_2 via ALD. For the deposition of HZO, similar chemicals were used for Zr, with some reports using the same type of precursor as for Hf and others mixing different types of precursors, including cocktail precursors that contain both Hf and Zr precursors in one bottle.[28]

$HfCl_4$ is one of the most prevalent Hf precursors for ALD, exhibiting a broad ALD window due to the high reactivity and low steric hindrance of the halide ligands. However, several disadvantages of halide precursors limit the applicability of $HfCl_4$ in low-temperature ALD processes.[34] Halide precursors are known to produce chlorine residue within the film, particularly at low-temperature range ALD, as well as reactive byproducts that can cause damage to the tool, particularly the pump.[73,74] In addition, the vapor pressure of solid precursors such as $HfCl_4$ is difficult to control and requires high-temperature heating to produce enough vapor to continue

the ALD process and prevent condensation on the gas lines. Multiple studies employed $HfCl_4$ and $ZrCl_4$ to deposit ferroelectric HZO films by supercycling two precursors, and the deposition temperature range was approximately 300 °C. Of these, some studies were able to achieve ferroelectricity from 450 °C to 300 °C by using halide-based precursors, electric field cycling, and annealing for a longer period of time in a furnace, as discussed in greater detail in the final chapter.[62,63,75]

TDMA and TEMA precursors have an ALD window between 200 °C and 300 °C, with a slightly higher temperature window for the TEMA precursors. This deposition temperature range is optimal for low-temperature ALD processes and the deposition of amorphous or nanocrystalline mixed HZO films, causing the majority of HZO ALD research to utilize these precursors. Kim et al., for instance, reported a comparative analysis of ALD, material, and electrical properties, including the dependability of ferroelectric HZO films deposited by TEMA-Hf/Zr and TDMA-Hf/Zr precursors.[64] Herein, 10 nm HZO films were deposited using a 1:1 ALD supercycle, which resulted in a 50:50 ratio of Hf and Zr within the films for both TEMA and TDMA precursors. The deposition temperatures for TEMA-Hf/Zr and TDMA-Hf/Zr were 280 °C and 260 °C, respectively, and ozone was used as the oxygen source. The growth rate of HZO using ozone was 0.12 nm per cycle with TEMA-Hf/Zr and 0.13 nm per cycle with TDMA-Hf/Zr, which is slightly faster. After TiN deposition for the top electrode and 450 °C rapid thermal annealing (RTA), grazing-incidence X-ray diffraction (GIXRD) confirmed the crystallization of both HZO. The larger grain size of TDMA-based HZO compared with TEMA-based HZO was caused by the higher carbon contamination of TEMA-based films, which inhibited grain growth. As a result, TDMA-based HZO exhibited a greater $2P_r$ and a smaller dielectric constant than TEMA-based HZO. In addition, the reliability of TDMA-based HZO

film was also superior to TEMA-based HZO, with a smaller wake-up effect, endurance up to 10^9 switching cycles, and lower leakage current.

Recent studies have utilized cyclopentadienyl (Cp)-based precursors with Hf and Zr for the deposition of ferroelectric HZO. This addition of Cp ligands permits the precursor to withstand a higher deposition temperature of greater than 350 °C, thereby shifting the ALD window to a higher temperature range of approximately 250 °C to 350 °C.[76–78] Increasing the deposition temperature of HZO films utilizing Cp-based precursors may appear counterproductive for low-temperature ferroelectric applications. However, employing a higher deposition temperature can produce a high-quality film with low impurity concentration and high density, resulting in low-temperature crystallization. Accordingly, Kim et al. demonstrated the benefit of using higher deposition temperatures by depositing HZO films with a cocktail precursor containing CpHf and CpZr.[60] For deposition, cocktail precursors with a molecular ratio of 35:65 for CpHf and CpZr, respectively, were used. For adequate vapor pressure, the precursor had to be heated and bubbled. The deposition temperature varied between 250 °C and 320 °C, and the growth per cycle ranged between 0.080 nm and 0.088 nm. After deposition, GIXRD confirmed the crystallization of Zr-rich films, which showed o and t-phase from 300 °C and increased with increasing deposition temperature. Following the same pattern, ferroelectric properties were observed in samples deposited at 300 °C, and a sample deposited at 320 °C exhibited a high $2P_r$ value with wake-up-free characteristics without post-metallization annealing (PMA). This result exemplifies how control of film properties can lead to low-temperature crystallization.

The combined result, which depicts the precursor dependence of $2P_r$ values as a function of process temperature based on recent literature, is shown in Figure 2b. Due to their compatibility with low deposition temperatures, TDMA- and TEMA-based precursors were the most widely

used for depositing low-temperature ferroelectric HZO films. Intriguingly, the overall trend of $2P_r$ values for low-temperature ferroelectric HZO films was not strongly related to the type of precursors unless a mixture of precursors was used to deposit the film. Due to the difficulty of optimizing deposition conditions for both precursors, mixing two distinct precursors to deposit HZO film results in a high amount of contaminants, leading to an increase in PMA temperature or degradation of ferroelectric properties. Correspondingly, this trend also emphasizes the significance of depositing high-quality films by optimizing the deposition process for high density and low impurity incorporation, thereby reducing the thermal budget for crystallization of the desired o-phase.

2.3 Oxygen source selection

As reported in the literature, common oxidants used to deposit ferroelectric HZO include water (H_2O),[49–54,56,58,66–68] ozone (O_3),[25,55,64,69] hydrogen peroxide (H_2O_2),[29] and oxygen (O_2) plasma[57,58]. Unlike other molecular oxygen sources, O_2 plasma consists of highly reactive oxygen radicals and ions, providing extra energy during reactions.[19,34,79,80] The additional energy supplied during the plasma cycle reduces the process temperature for ALD reaction and enhances the crystallization of plasma-enhanced ALD (PEALD) compared to TALD.[57,58] However, unlike TALD, the anisotropic nature of the plasma source is difficult to implement in complicated 3D structures and can produce a thick interfacial layer due to excessively strong oxidation power.[74,81,82] Consequently, the use of TALD is preferable to deposit a thin film on complex 3D structures conformally and minimize interface formation. Therefore, this section focuses on oxygen sources that are mainly used in TALD processes. This section demonstrates the impact of oxygen sources on ALD growth characteristics, and electrical/material properties. In addition, various examples from many reports utilizing H_2O, O_3, and H_2O_2 as oxygen sources

to deposit HZO film are introduced. Furthermore, the oxidant dependence of HZO ferroelectric properties and the crystallization temperature required to obtain ferroelectric o-phase is discussed.

H_2O is the most popular oxygen source for ALD deposition of HZO due to its high vapor pressure, ease of accessibility, and compatibility with a wide range of deposition temperatures. Due to its low oxidation power compared with that of O_3, H_2O is gentler on the substrate, minimizing interface formation.[81,83] However, the low oxidation power of H_2O can be a disadvantage, leaving unreacted precursors behind, resulting in residual contamination and necessitating a higher temperature for thin films of superior quality.[84] Due to these factors, H_2O may not be the optimal oxygen source for low-temperature applications, as is the case with other reactive oxygen sources. As depicted in Figure 2c, numerous reports have demonstrated that H_2O can deposit low-temperature ferroelectric HZO films with relatively lower $2P_r$. In addition, O_3 was a common oxygen source for TALD, as it is easier to purge than sticky H_2O and has a potent oxidizing capacity. The strong oxidation power of O_3 enables it to react with the residual carbon, while ALD synthesizes a high-quality film with a small amount of hydrogen relative to H_2O.[69,85] In contrast, when utilizing O_3, the interface formation and step coverage dependence of substrate temperature caused by oxygen radical recombination must be carefully considered.[31,81,85] Using TALD with TDMA-Hf, H_2O, and O_3, Kim et al. demonstrated the effect of oxygen source on the ferroelectric properties of HZO capacitors.[69] After TiN/HZO/TiN stack fabrication, and 400 °C RTA, both H_2O- and O_3-based HZO crystallized to the o-phase, as confirmed by GIXRD. Both HZO capacitors exhibited large $2P_r$ values of 47.3 μC/cm^2 for O_3-based HZO capacitors and 38.7 μC/cm^2 for H_2O-based HZO capacitors. In addition, H_2O-based HZO showed a higher leakage current and a lower breakdown field, indicating less reliable properties than O_3-based HZO. It was confirmed that when H_2O was used as an oxygen source, the hydrogen content in the film

measured by dynamic secondary ion mass spectrometry (DSIMS) was higher compared to O_3-based films, while crystal structure, carbon contamination, and vacancy concentration were similar. Thus, showing the impact of hydrogen on the ferroelectric properties and reliability and suggesting the importance of oxidant selection for robust low-temperature ferroelectric properties of ALD HZO.

As shown in the findings of Kim et al., hydrogen incorporation degrades the material and electrical properties. The majority of hydrogen within the film exists as hydroxyl, potentially reducing the film density by terminating the oxygen bond with hydrogen preventing it from forming metal-oxygen bonds. Therefore, selecting an oxygen source that produces HZO films with low hydrogen content and high density using ALD is one of the most crucial aspects of achieving superior electrical properties. Very few studies with HfO_2 and HZO ALD have shown that H_2O_2 produces dense, highly stoichiometric films that are ideal for low-temperature applications.[29,86] H_2O_2 has comparable oxidation power to O_3 and lower dissociation energy on O-O bonds (2.22 eV) than the O-O bond (3.77 eV) of O_3, allowing it to react readily with the precursors.[87,88] In addition, H_2O_2 is readily available in large quantities as a liquid that can be incorporated into the ALD system without any safety concerns. In this regard, Choi et al. reported the ALD and HfO_2 film characteristics of 50 wt.% H_2O_2 as an oxygen source reacting with TEMA-Hf versus H_2O.[86] Between 175 to 325 °C deposition temperatures, the ALD window was determined to be below 300 °C for both H_2O and H_2O_2. The growth rate and dielectric constant were similar between the two oxidants. However, the leakage current of the H_2O_2-based HfO_2 capacitor was an order of magnitude lower than that of the H_2O case. X-ray photoelectron spectroscopy (XPS) results showed that the H_2O_2-based HfO_2 film had a smaller full-width half maximum of Hf 4f spectra than the H_2O-based HfO_2 film, indicating a stoichiometric film with a

smaller amount of suboxide. In addition, 90% conformality over a high aspect ratio (~15) structure was demonstrated using H_2O_2.

However, most commercially available H_2O_2 is diluted with H_2O to extend its shelf life, and pure H_2O_2 has a very short shelf life before decomposing into H_2O and O_2. Furthermore, compared with the boiling point of H_2O (100 °C), H_2O_2 has a higher boiling point (150.2 °C), resulting in a very low partial pressure of H_2O_2 within the vapor, thereby limiting the amount of H_2O_2 supplied to the ALD. In addition, H_2O evaporates faster from the aqueous solution of H_2O_2, causing a continuous increase in the partial pressure of H_2O_2. This makes the amount of H_2O_2 delivered to the system difficult to control, thereby resulting in inconsistent film properties.[89–91] Jung et al. circumvented this issue with a specially designed vaporizer that generated anhydrous H_2O_2 to study the effect of H_2O_2 on the ferroelectric property and the process temperature while removing the H_2O effect.[29] Utilizing TDMA-Hf/Zr with H_2O_2 at 250 °C, H_2O_2 was able to produce amorphous HZO films with faster growth, higher density, and etch resistance than O_3. After 350 °C PMA, H_2O_2-based HZO capacitors exhibited a $2P_r$ value of 55 $\mu C/cm^2$, whereas O_3-based HZO capacitors exhibited a $2P_r$ value of 10 $\mu C/cm^2$. Moreover, compared with O_3-based HZO capacitors, the H_2O_2-based HZO capacitors demonstrated a lower leakage current, higher breakdown voltage, and wake-up-free behavior with increased endurance up to 10^{10} cycles. GIXRD confirmed the complete crystallization of H_2O_2-based HZO films, while O_3-based HZO films were near an amorphous state with small crystals. Subsequently, it was asserted and confirmed by XPS and DSIMS that the H_2O_2-based HZO films had a smaller amount of non-lattice oxygens and a reduced hydrogen content, which led to these enhanced properties. Therefore, for the synthesis of high-quality films via chemical densification for low-temperature ferroelectric applications, oxygen source selection is crucial.

The studies reported in this section demonstrated that chemical densification could lower the crystallization temperature by creating a dense amorphous film. Moreover, the dense film with o-phase and t-phase nanocrystalline seed can provide nucleation sites that enable the growth of crystalline o-phase with less energy and a faster nucleation rate, thereby reducing the thermal budget. As mentioned in the report by Materano et al., these dense, stoichiometric HZO films may not be favorable for the formation of the o-phase.[38] However, the amount of oxygen in the film is not the only factor to promote o-phase formation. Therefore, controlling other factors that can promote the phase transition to o-phase (e.g., doping, interface, stress, etc.), dense and stoichiometric HZO film can still deliver robust ferroelectricity. Consequently, the fabrication of a stoichiometric HZO film that is close to the ideal condition by TALD can facilitate both low-temperature crystallization and a high o-phase fraction for improved ferroelectricity. Figure 2c depicts the relationship between process temperature and $2P_r$ values based on the oxygen source. Process temperature around 300 °C, O_2 plasma showed the best results with high $2P_r$, and H_2O achieved $2P_r$ around 24 μC/cm^2, exactly the IRDS FRAM limit, using TEMA cocktail precursors with Zr-rich composition.[58,71] Additionally, in the low-temperature regime below 400 °C, H_2O_2-based HZO films had the highest average $2P_r$, followed by O_3-based HZO films with slightly lower but still high $2P_r$, and H_2O-based HZO films with the lowest average $2P_r$.[29] Based on the trend, achieving ferroelectricity below 300 °C was difficult using TALD with conventional annealing techniques such as RTA. Thus, to further lower the process temperature for BEOL-compatible ferroelectrics, an additional energy source, plasma, will be discussed in the next chapter.

Figure 2.

2.4 Plasma Enhanced Atomic Layer Deposition

Figure 3.

The low-temperature fabrication of ferroelectric $Hf_xZr_{1-x}O_2$ (Hf:Zr = 0.43:0.57; HZO) films has been studied via PEALD using a Hf/Zr cocktail precursor and PMA processes.[57,58] The HZO film deposited by TALD using H_2O or O_3 as an oxidant gas typically has an amorphous structure.[92] On the other hand, PEALD process utilizing O_2 plasma was focused due to its strong oxidation power and high energy ion/electron bombardment. First, the effect of an oxidant gas on the crystallization of the as-grown HZO films prepared via the ALD process at 300 °C was investigated. The as-grown HZO film with H_2O gas deposited via TALD exhibited an amorphous-like structure because few nanocrystals were observed near the surface of the TiN bottom electrode (BE-TiN), and a small diffraction peak from the (111) plane of the o/t/c-phases was observed at $2\theta \approx 30.5°$ (Figure 3a). However, for the as-grown HZO film with O_2 plasma gas deposited via PEALD, the peak of the (111) plane of o/t/c-phases increased, and partially crystallized ~5 nm grains were observed (Figure 3b). In addition, both HZO films after PMA treatment at 300 °C retained the conformation and uniformity between the TiN top electrode (TE-TiN) and the BE-TiN. Moreover, they exhibited a polycrystalline structure with a grain size of 10–20 nm and consisted predominantly of o/t/c-phases. During the annealing and deposition processes of TiN and HZO films, an interfacial layer such as TiO_2, TiO_x, or TiO_xN_y was easily formed because the TiN could scavenge oxygen atoms from the HZO film.[93–98] In addition, the formation of oxygen vacancies in the HZO film and interlayer may result in a high leakage current and a reduction in the endurance properties.[55,99,100] Even at 600 °C, transmission electron microscopy (TEM) and energy-dispersive X-ray spectroscopy (EDS) analysis confirmed that the interface between the TALD HZO film and BE-TiN was abrupt due to negligible reaction and diffusion during the deposition and annealing processes.[101–103] Our lower-temperature annealing

process at 300–400 °C is anticipated to inhibit further atomic diffusion and chemical reaction at the TiN/HZO interface of metal-ferroelectric-metal (MFM) capacitors fabricated with the TALD and PEALD HZO films.

Figure 4.

Figure 5.

Various analysis techniques have determined the absolute ratio of the ferroelectric o-phase in HZO films. However, in GIXRD analysis, deconvoluting the peak at $2\theta \approx 30.5°$ into separate peaks for the o-, t-, and cubic phases (c-phase) is difficult due to the proximity of the peak positions. Therefore, to determine the absolute ratio of the ferroelectric o-phase of HZO films, synchrotron grazing-incidence wide-angle X-ray scattering (GIWAXS) analysis was attempted.[58] Figures 4a and 4b display examples of spectra generated by conventional Rigaku GIXRD with Cu Kα source (1.5418 Å) and GIWAXS with synchrotron source (0.77009 Å). The synchrotron GIWAXS condition was configured with a microbeam (cross-sectional diameter of 2 μm) to reduce the X-ray footprint on the sample to resolve higher q peaks, resulting in a high-resolution d-spacing analysis, as shown in Figure 4b.[104] Furthermore, because of the short wavelength, ultrabright, and highly collimated beam of a synchrotron source, synchrotron-based GIWAXS can be performed with an incidence angle $<0.1°$, allowing for surface-sensitive, high-resolution d-spacing analysis (Figure 4c).[105] Figures 5a and 5b show the synchrotron GIWAXS patterns of TALD and PEALD HZO films prepared with and without the PMA process at 300–400 °C. GIWAXS analysis was performed on each sample after the TE-TiN was etched to eliminate its associated diffraction peaks. The GIWAXS data for the TALD and PEALD HZO films without the PMA process exhibited broad diffraction peaks at a d-spacing of 2.93 Å; these peaks were

assigned to the mixed o(111)/t(101)/c(111)-phases, indicating that both as-grown films formed nanocrystals with o/t/c-phases, in accordance with the TEM analysis results. Large peaks originating from o/t/c-phases were observed in the pattern of PMA-treated samples, whereas the peaks of the m-phase were weak. Notably, the peak position of the o/t/c-phases for both the TALD and PEALD HZO films gradually shifted to a larger d-spacing region as the PMA temperature rose from 300 °C to 400 °C; however, almost no peak shift was observed in the laboratory-based GIXRD patterns. It is well known that the d-spacings of the crystal structures of HfO_2 and ZrO_2 increase in the order c < t < o. As the annealing temperature increased, these peak shifts suggest that the formation of the o-phase was favored over the formation of the c- and t-phases. During the annealing process, TiN electrodes have been reported to subject HZO films to tensile stress, promoting the formation of the metastable ferroelectric o-phase.[24,106] As the annealing temperature increases, greater mechanical stress is applied to the HZO films by the TiN electrodes, resulting in the formation of the o-phase. A moderate addition of oxygen vacancies can also facilitate the formation of the ferroelectric o-phase.[37] Moreover, the GIWAXS spectra of PEALD HZO films exhibited a larger peak shift than those of TALD HZO films, indicating that the ferroelectric o-phase formed more readily in PEALD HZO films than in TALD HZO films. This also indicates that the nanocrystalline o/t/c-phases in the as-grown HZO film are crucial in forming the ferroelectric o-phase.

Figure 5c shows the correlation between the $2P_r$ value (extracted from polarization–electric field (P–E) hysteresis curves for pristine samples) and the d-spacing of o(111)/t(101)/c(111)-phases (extracted from the synchrotron GIWAXS data) for the TALD and PEALD HZO films following PMA process at 300–400 °C, during which the d-spacing increased with increasing annealing temperature. The $2P_r$ values of TALD and PEALD HZO films increased linearly with

increasing d-spacing for o(111)/t(101)/c(111). The maximum $2P_r$ value and d-spacing (35 μC/cm^2 and 2.99 Å, respectively) were obtained for PEALD HZO films subjected to PMA at 400 °C. In addition, the theoretical d-spacing of the o-phase in HZO (Hf:Zr = 0.43:0.57) films is 2.99 Å, as estimated using the d-spacings for HfO_2 (2.96 Å) and ZrO_2 (3.01 Å) according to Vegard's law. These results indicate that a nearly ideal ferroelectric phase was achieved in the HZO film deposition via the PEALD process followed by the PMA process at 400 °C. Notably, an asymmetric peak shape indicates that the films still contain a certain fraction of the nonferroelectric t- and c-phases, albeit a small fraction compared with the dominant o-phase. The results demonstrate that synchrotron GIWAXS allowed for the precise analysis of the crystal structure of ferroelectric HZO films, revealing the crucial relationship between their ferroelectricity and crystal structure.

Figure 6.

Figures 6a and 6b show the P–E hysteresis curves of MFM capacitors with 10-nm-thick TALD and PEALD HZO films, respectively. In addition, Figure 6c depicts the relationship between the PMA temperature and the $2P_r$ value derived from the P–E hysteresis curves of the TALD and PEALD HZO films. Lattice fringes with different orientations are observed (Figure 3b), indicating that a nanocrystalline structure with o/t/c-phases and a grain size of ~5 nm was partially formed. Consequently, the switching curve of the as-grown HZO film fabricated via the PEALD process showed a $2P_r$ value of 1.7 μC/cm^2. In contrast, linear paraelectric-like behavior was observed for the as-grown HZO film fabricated via the TALD process owing to its amorphous-like structure with few nanocrystals (Figure 3a). After the PMA process at 300 °C, the PEALD HZO film crystallized completely and formed a polycrystalline structure with grain sizes between 10 and 20 nm. The TALD HZO film, in contrast, retained a portion of the

amorphous-like structure region. The nanocrystal grains formed during the PEALD process play a crucial role as nuclei for the crystallization of HZO films, forming a fully crystallized HZO film with a low thermal budget even at 300 °C.[57,58] The full crystallization observed after the PMA process at 300 °C resulted in a large hysteresis loop with a $2P_r$ value of 29 μC/cm^2 in the P–E curve of the PEALD HZO film, which was approximately 1.2 times greater than that (24 μC/cm^2) in the P–E curve of the TALD HZO film. Furthermore, the $2P_r$ value of both the TALD and PEALD HZO films increased with increasing PMA temperature due to the improved crystallinities; for example, complete crystallization of the TALD HZO film was confirmed when the annealing temperature was increased to 400 °C, whereas the PEALD HZO film was already fully crystallized after the 300 °C PMA process due to the nucleation effect of the nanocrystals formed after the PEALD process. Consequently, after annealing at 400 °C, the TALD and PEALD HZO films attained similar $2P_r$ values of 33 and 35 μC/cm^2, respectively. Therefore, a greater $2P_r$ value was obtained at a lower process temperature region using the PEALD method.

Figure 6d shows the endurance properties of MFM capacitors prepared with TALD and PEALD HZO films via the PMA process at 300 °C and 400 °C. Positive-up negative-down (PUND) measurements were performed to determine the switching polarization (P_{sw}) value during field cycling. The PUND method comprised two positive and two negative triangle pulses with the same triangle voltage pulse (25 μs rise time and 25 μs fall time) at ± 3.0 MV/cm used in the P–E measurements and a 25 μs delay time. In the pristine state of 100 field cycles, the PEALD HZO films had higher P_{sw} values than the TALD HZO films when exposed to the same PMA temperature conditions, as shown in Figure 6d. All TALD and PEALD HZO films exhibited a wake-up effect until 10^3–10^4 field cycles, consistent with previously reported results.[100,107–109]

After wake-up field cycling, the P_{sw} values of the TALD and PEALD HZO films annealed at 300 °C increased by ~15% compared with their pristine values. However, the films annealed at 400 °C showed a reduced wake-up increase (~7%). During wake-up field cycling, it has been reported that the nonferroelectric t-phase transforms into the ferroelectric o-phase, increasing the P_{sw} value.[99,110–112] According to synchrotron GIWAXS data, the reduced wake-up effect observed in TALD and PEALD HZO films subjected to PMA at 400 °C is attributable to these films having a higher proportion of ferroelectric o-phase (larger d-spacing of the o(111)/t(101)/c(111)-phases).

3. INTERFACE ENGINEERING

Figure 7.

Other approaches for fabricating ferroelectric HZO films have been studied. The difference in thermal expansion coefficients between TiN and HZO films is promising for forming the ferroelectric o-phase during the annealing process.[24,106] In MFM ferroelectric memory, the HZO film is sandwiched by TiN; as a result, this difference in thermal expansion coefficients has a remarkable impact. However, Si channel in the metal-ferroelectric-semiconductor (MFS) ferroelectric transistor, an amorphous SiO_2 interfacial layer (SiO_2-IL) is easily formed between an HZO film and Si, which could cause stress relaxation, whereas a Si substrate is expected to play a role as a tensile stressor to HZO films during an annealing process. Furthermore, it has been reported that MFS structures require a high-temperature process (>400 °C) to achieve robust ferroelectricity.[113,114] This high temperature potentially leads to the excessive growth of SiO_2 at the interface and causes reliability issues on MFS capacitors and FeFETs.[13,115–117]

Moreover, high process temperature also poses limitations for low thermal budget applications (e.g., 3D integration and flexible electronics) that require channel materials like oxide semiconductors.[118–120] A new idea was proposed by Onaya et al. using a ZrO_2 nucleation layer to form the HZO film with the ferroelectric o-phase in an MFS structure.[121] This concept is based on the superior characteristics of ZrO_2 films processed via the low-temperature ALD process at 300 °C (e.g., good crystallinity and predominantly o/t/c-phases). The HZO-based MFM capacitors with a ZrO_2 nucleation layer exhibited the improvement of their ferroelectricity, while those with an amorphous Al_2O_3 layer showed smaller $2P_r$ compared to the conventional HZO-based MFM capacitors.[101–103,122–124] Here, the effect of the ZrO_2 layer on the ferroelectricity of the MFS structure was investigated. Figures 7a and 7b show cross-sectional TEM images of MFS capacitors without ZrO_2 (w/o) and ZrO_2-10-nm following the PMA process at 300 °C. Due to the low thermal budget of 300 °C, a suppressed SiO_2-IL with a thickness of one or two monolayers (0.3–0.6 nm) was formed between the HZO film and the Si substrate for both capacitors. These SiO_2-ILs were thinner than those at the interface of a HfO_2-based film and a Si substrate (≥1 nm).[114,125–128] A few nanocrystals with a grain size of 5–10 nm partially formed in the HZO film of the w/o capacitor, while most of the film remained amorphous. In contrast, the HZO film of the as-grown ZrO_2-10-nm capacitor was fully crystallized with the same orientation as the ZrO_2 grains, and grain size ranged from 10 to 20 nm. TEM–EDS analysis determined that the interface between the top ZrO_2 and HZO films was abrupt due to less diffusion and reaction between these films during the PMA process. The GIXRD patterns for the PMA-treated w/o and the as-grown ZrO_2-10-nm MFS capacitors are shown in Figure 7c. The patterns of both capacitors exhibit a sharp diffraction peak of the (111) planes of TiN at $2\theta \approx 36.7°$. Moreover, no clear peak originating from the HZO film was observed, indicating that the HZO film formed a

predominately amorphous structure, consistent with the results of the TEM analysis (Figure 7a). However, the GIXRD pattern for the as-grown ZrO_2-10-nm capacitor displayed diffraction peaks at 2θ≈30.7° and 35.6°, which were assigned to mixtures of o(111)/t(101)/c(111)- and o(002)/t(110)/c(200)-phases, respectively; no peak of the paraelectric m-phase was observed. Even with a low thermal budget of 300 °C, a crystallized HZO film consisting of the ferroelectric o-, t-, and c-phases was obtained using a top ZrO_2 nucleation layer. Because the lattice constants for the ferroelectric o-phase and the nonferroelectric t- and c-phases are similar, it is challenging to identify the diffraction peak originating solely from the o-phase in HZO thin films using laboratory-based XRD measurements.[58] Even after the ALD process, the top ZrO_2 nucleation layer of the as-grown ZrO_2-10-nm capacitor was crystalline and comprised o-, t-, and c-phases, while the HZO film exhibited an amorphous structure, as determined using GIXRD analysis. Therefore, the polycrystalline ZrO_2 film following the ALD process played a crucial role as a nucleation layer for the crystallization of the HZO film and formation of the ferroelectric o-phase during the 300 °C low-temperature PMA process.

To evaluate the P_{sw} during field cycling, PUND measurements were performed. Figures 7d and 7e show the endurance properties, where the P_{sw} was extracted using the PUND method for the w/o MFS capacitor, ZrO_2-2-nm, and ZrO_2-10-nm MFS capacitors, following the PMA process at 300 °C. During field cycling, the triangular voltage consisted of positive and negative pulses with a pulse width of 50 μs at ± 4 MV/cm; a 25 μs delay time was applied. The pulse sequence in the PUND method comprised two positive and two negative triangular pulses with the same pulse conditions as described above (insets, Figure 7d). The $+P_{sw}$ value was estimated using two positive pulses of P and N, whereas two negative pulses of N and D were used to estimate the $-P_{sw}$ value. The $+P_{sw}$ value was lower than the $-P_{sw}$ value for each capacitor,

possibly due to the voltage drop caused by the depletion layer in the Si substrate.[129] The ZrO_2-10-nm capacitor exhibited hard breakdown after field cycling for 3×10^5 cycles, consistent with the previous reports on HfO_2-based MFS capacitors, whereas the w/o and ZrO_2-2-nm capacitors continued to function even after 10^6 cycles.[121] The earlier breakdown of the ZrO_2-10-nm capacitor is attributed to its lower breakdown field compared with the w/o and ZrO_2-2-nm capacitors, resulting from the fully crystallized ZrO_2/HZO bilayer with a polycrystalline structure. As a result of the wake-up effect, the $+P_{sw}$ and $-P_{sw}$ of the w/o capacitor increased by as much as ~10% after 10^2–10^3 field cycling cycles compared with the pristine state, whereas the ZrO_2-2-nm and ZrO_2-10-nm capacitors exhibited no wake-up effect. Across all capacitors, the degradation of the $-P_{sw}$ during field cycling was substantial, whereas the degradation of the $+P_{sw}$ was minimal. After 10^3 wake-up cycles, the $-P_{sw}$ of the w/o capacitor drastically decreased by 15% per decade of cycles. Moreover, a comparison of the performance of the ZrO_2-2-nm and ZrO_2-10-nm capacitors with wake-up-free properties reveals that the $-P_{sw}$ for both capacitors decreased linearly and that the ZrO_2-10-nm capacitor could reduce the $-P_{sw}$ degradation ratio by ~5% per decade of cycles, as estimated during field cycling between 10^0 and 10^5 cycles, whereas the ZrO_2-2-nm capacitor could reduce the $-P_{sw}$ degradation ratio by ~10% per decade of cycles.

Two potential causes were considered for the wake-up effect for the w/o capacitor. One possible cause is the poor crystalline quality of the HZO film (Figure 7). During field cycling, the nonferroelectric t-phase, which forms preferentially between the TiN electrode and the HZO film, is reported to transform into the ferroelectric o-phase, increasing P_{sw}.[111,130,131] The other cause is oxygen vacancies at the TiN/HZO interface. It has been hypothesized that oxygen vacancies are generated preferentially at the TiN/HZO interface due to a scavenging effect of TiN during deposition and annealing.[132–134] Generally, these oxygen vacancies are thought to be

one of the key factors to cause the wake-up effect for HfO_2-based materials because of a reduction in the local built-in bias field and phase transformation from a non-ferroelectric phase to ferroelectric o-phase caused by a uniform redistribution of oxygen vacancies during field cycling.[99,100,135] Hard X-ray photoelectron spectroscopy analysis confirmed that a TiO_xN_y IL (TiO_xN_y-IL) was formed at the interface between the TE-TiN and the HZO film in the TiN/HZO/TiN MFM capacitor after the PMA process at 300 °C; this interfacial layer could lead to the formation of oxygen vacancies at the TiN/HZO interface (results not shown). For the wake-up-free properties of the ZrO_2-2-nm and ZrO_2-10-nm capacitors, two alternative explanations were proposed. Because of the ZrO_2 nucleation effect, the HZO film preferentially forms the ferroelectric o-phase rather than the nonferroelectric phase, which causes a phase transformation during field cycling.[102,122] Introducing a ZrO_2 nucleation layer contributes to the stabilization of the ferroelectric o-phase in HfO_2-based thin films, according to first-principles calculations.[136] The second explanation is that inserting a ZrO_2 nucleation layer between the TE-TiN and the HZO film can prevent the formation of oxygen vacancies at the ZrO_2/HZO interface because the ZrO_2 film disrupts the TiN scavenging effect, which in turn does not affect the HZO film. Consequently, these capacitors exhibited wake-up-free endurance properties. Next, the minimal decrease in $+P_{sw}$ observed during field cycling for all capacitors was evaluated. During the PMA process at 300 °C, the thickness of SiO_2-IL was unaffected. Speculation suggests that, unlike the scavenging effect of TiN, oxygen diffusion into the SiO_2-IL does not occur during the PMA process, and, as a result, the formation of oxygen vacancies at the HZO/SiO_2-IL interface can be suppressed.

Regarding the degradation mechanism of $-P_{sw}$, two types of oxygen vacancy behavior were observed. During the fabrication process, oxygen vacancies formed on the top surface of the

HZO film (i.e., the TiN/HZO interface for the w/o capacitor and the ZrO_2/HZO interfaces for the ZrO_2-2-nm and ZrO_2-10-nm capacitors). The ZrO_2 film must reduce the number of oxygen vacancies at the TiN/HZO interface because the HZO film is distant from the TiN/ZrO_2 interface, which is the source of oxygen vacancies. In addition, the ZrO_2-10-nm capacitor with the thickest ZrO_2 film displays the greatest effect. Secondly, during field cycling, additional oxygen vacancies are generated along the grain boundaries of the HZO film.[99,100] For the ZrO_2-10-nm capacitor, larger grains were observed (Figure 7), decreasing the number of grain boundaries.[102] Based on these results, HZO-based MFS capacitor with a 10-nm-thick top ZrO_2 nucleation layer exhibited superior ferroelectric and wake-up-free properties, and higher fatigue resistance, even at a low thermal budget of 300 °C. However, the effects of antiferroelectric ZrO_2 on the switching properties and reliability of the antiferroelectric-ZrO_2/ferroelectric-HZO bilayer remain unclear, and additional research is required before these bilayers can be utilized in future ferroelectric memory devices.

4. STRESS AND THERMAL PROCESS

The ferroelectric properties of HfO_2-based films are known to originate from the noncentrosymmetric o-phase.[10,22] However, HfO_2-based films crystallized under standard semiconductor process conditions have a stable m-phase.[10,22] For this reason, numerous reports have aimed at simultaneously promoting o-phase formation and suppressing m-phase.[10,22] According to previous studies, annealing with a capping layer (i.e., PMA) is crucial.[10,22,24] During crystallization, the capping layer (i.e., the top electrode) induces tensile stress in the in-plane direction, thereby preventing the formation of an undesirable nonpolar m-phase (i.e., stress-induced crystallization).[24,106,132] Meanwhile, RTA, which performs annealing at a specific temperature for a very short time, has been widely utilized to crystallize HfO_2-based films.[10,22]

In 2017, Kim et al. reported on the ferroelectricity of TiN/HZO/TiN capacitors with 10 nm HZO films annealed either before (i.e., postdeposition annealing, PDA) or after (i.e., PMA) TE-TiN deposition at various annealing temperatures (300–500 °C) using an RTA system.[24] PDA-HZO samples exhibited no ferroelectric behavior at any temperature, whereas PMA-HZO samples exhibited explicit ferroelectric behavior above 400 °C. In addition, the ferroelectric polarization was enhanced when annealed PMA-HZO samples with a TE-TiN of sufficient thickness (>90 nm) were used. By measuring the change in curvature before and after annealing, it was found that the estimated tensile stress increased as the thickness of the TE-TiN increased. These results indicate a clear tensile stress effect of the top electrode under the PMA condition and suggest that ferroelectric behavior can be obtained even at a low annealing temperature of 400 °C by controlling the stress from the top electrode during the PMA process. This stress-controlled low-temperature ferroelectric behavior can be distinguished from low-temperature crystallization driven by densification. Both HZO films with and without the TE-TiN crystallized after 400 °C PMA, given that the amorphous film density and activation energy for crystallization were identical.[24,137] Thus, the stress conditions influence the energy of the phases, decreasing the o-phase energy and increasing the driving force for phase transformation into o-phase rather than m- or t-phase.[4] Therefore, the ratio of the o-phase will be dominant under stronger stress at the same PMA temperature, demonstrating how stress control can be used to achieve improved ferroelectric properties at lower temperatures. As demonstrated above, in the year 2017, the lowest reported annealing temperature for fluorite-structure ferroelectrics with high $2P_r$, using the TALD and simple RTA process, was 400 °C.[24] Nevertheless, this annealing temperature impedes the incorporation of HZO thin films into BEOL processes.[22] For this

reason, numerous attempts have been made to reduce the annealing temperature required to crystallize HZO thin films during the PMA process to less than 400 °C.[22,25,26,63]

Figure 8.

Recently, a simple method to increase the annealing time has been proposed to reduce the annealing temperature below 400 °C based on the thermal budget of HZO thin films.[26,63,138] Thermal budget, which is a concept represented by a relationship between an annealing temperature and an annealing time, generally refers to the total amount of heat applied to a device during an annealing process. Cho et al. investigated the ferroelectric properties of 10-nm-thick HZO thin films crystallized (via the PMA process) at various annealing temperatures (350–500 °C) and times (1–5 hours) using a furnace instead of RTA.[26] Figure 8 shows the schematics of various furnace annealing processes and the resulting P–E hysteresis curves for TiN/HZO/TiN capacitors. Similar to previous results,[10,22,24,69] PMA-HZO samples exhibited ferroelectric properties at temperatures above 400 °C regardless of annealing time but not at temperatures below 400 °C. However, as the annealing time increased, ferroelectric behavior appeared, and the PMA-HZO sample annealed at 350 °C for more than 4 hours showed a large polarization comparable to the PMA-HZO sample annealed at 400 °C for 1 hour. Furthermore, the reduced annealing temperature can improve the endurance properties of the PMA-HZO sample by reducing the formation of oxygen vacancies within the HZO thin film or at the interface with the electrodes. These results indicate that, even at temperatures as low as 350 °C, increasing annealing times can achieve the required robust endurance and sufficient polarization values for FRAM applications. In other words, it suggests that a certain thermal budget, considering annealing temperature and time, is necessary to obtain ferroelectric properties in HZO thin films. Additionally, Lehninger et al. reported that ferroelectric properties of HZO thin films could be

obtained through prolonged annealing in a low-temperature furnace below 400 °C, reaching down to 300 °C.[63,120] XRD analysis confirmed that the ferroelectric phase formed in the HZO thin film even at annealing temperatures below 400 °C when the annealing time was increased. These approaches utilize annealing time to compensate for the slow nucleation rate at low temperatures to obtain ferroelectricity with a low annealing temperature. Moreover, this demonstrates that stress control would only reduce the o-phase energy, rather than the activation energy, to increase the nucleation rate and decrease the crystallization temperature. Despite achieving a low temperature of less than 400 °C, the crystallization method using such a furnace requires a lengthy process time of several hours or longer. However, the existing thermal budget during interconnect formation can be leveraged to crystallize HZO films without the need for a separate crystallization step, potentially saving time and cost in the BEOL fabrication process.[75]

Figure 9.

From this point of view, as a way to reduce the thermal budget (i.e., reducing both the annealing temperature and time), a high-pressure annealing (HPA) method capable of increasing the pressure during the annealing process and employing a capping layer (i.e., a PMA process) was recently introduced.[25] Previous HPA studies have focused more on improving the ferroelectric properties of HZO thin films by promoting o-phase formation than on the crystallization temperature. The improved ferroelectric properties of the PMA-HZO sample could be obtained at the same annealing temperature by substituting the conventional RTA process with high-pressure nitrogen annealing.[139] In particular, as the annealing pressure increased up to 50 atm at 450 °C, the o-phase ratio increased gradually, and a large ferroelectric polarization with robust endurance was obtained. Meanwhile, a method for improving ferroelectric properties by controlling oxygen vacancies in the HZO thin film was proposed by

additionally executing the HPA process before the RTA process.[140] In this case, the deposited HZO thin film was first subjected to high-pressure oxygen annealing at 250 °C, and then the RTA process was performed again at 500 °C after depositing the TE-TiN (i.e., PMA process). As a result, it was confirmed that the ferroelectric polarization was improved when HPA (oxygen pressure of 40 atm) was added compared to the HZO sample annealed using only RTA. Meanwhile, it was recently reported that the ferroelectric behavior of HZO thin films could be obtained at temperatures below 400 °C via the PMA process using only HPA. Kim et al. investigated the effect of annealing pressure and time on the crystal structure and ferroelectric properties of HZO thin films via HPA (15 atm N_2 pressure), RTA, and furnace processes at 300 °C.[25] In the case of the HPA and furnace processes, the TiN/HZO/TiN capacitors were placed in each chamber preheated to 300 °C in an N_2 atmosphere and removed immediately after the annealing process for at least 30 min to enable rapid cooling as in the general RTA process (see Figure 9). Consistent with previous findings, HZO thin films annealed at 300 °C in an RTA or furnace process did not crystallize or exhibit ferroelectric behavior.[24,26,69] Considering the thermal budget of HZO thin films, a longer annealing time at 300 °C may be required to obtain ferroelectricity via o-phase formation. However, when an N_2 pressure of 15 atm was applied, the HZO thin film crystallized even at a low-temperature of 300 °C, exhibiting a sufficiently large ferroelectric polarization. Interestingly, the thickness of the HPA HZO thin film decreased during the crystallization process, indicating that the driving force for phase transformation from low-density amorphous to high-density crystalline increased even at 300 °C as the annealing system pressure increased to 15 atm. Consequently, the HPA process is a helpful strategy for attaining the ferroelectric properties of sub-10 nm HZO films even with limited thermal budgets.

In summary, it was difficult to form the o-phase of the HZO thin film at annealing temperatures below 400 °C using a TE-TiN that induces tensile stress via the PMA process. However, by increasing the annealing time based on the thermal budget or applying pressure during the annealing process, HZO thin films could be crystallized even at low temperatures (<400 °C), thereby acquiring ferroelectric properties. Remarkably, the HPA process can overcome the high thermal budget (≥400 °C) of a typical RTA process and simultaneously solve the problem of long annealing time, which is a drawback of the furnace-based low-temperature process. In other words, HPA can be a helpful method for low-temperature processes that have posed a persistent obstacle to integrating HfO_2-based films into BEOL.

5. CONCLUSIONS

This review has highlighted the role of ALD techniques and recent advances in low-temperature HfO_2-based ferroelectrics, particularly HZO-based materials, which have emerged as promising materials for BEOL-compatible next-generation nonvolatile memory devices. The primary challenge is stabilizing the metastable ferroelectric o-phase in sub-10 nm-thick films at low temperatures by controlling different parameters that can lower the energy barrier and increase the crystallization driving force. Various strategies have been developed to achieve this objective, including doping, precursor and oxidant source selection, deposition temperature control, interface modification, stressor design, and pressurized annealing techniques. These approaches aim in two directions: optimizing ALD conditions for high-quality film deposition and applying additional stress and strain to promote the formation of o-phase with a limited thermal budget. Following these directions, this review provides insight into various chemical and physical densification strategies for producing high-quality films with high density and low impurity concentration to boost crystallization and electrical performance. As evidenced by

dense H_2O_2-based films, nanocrystalline seeded HZO films with deposition temperature control, PEALD, and interface engineering, the densification approach can affect the kinetics of phase transition and potentially lower the energy barrier from amorphous to the o-phase, resulting in a low crystallization temperature. In addition, engineering a stress and strain-controlled environment to stabilize the o-phase to a lower energy state could increase the driving force to the o-phase rather than transforming into other nonferroelectric phases such as m-, t-, and c-phase, thereby achieving o-phase dominant films at low temperatures. For instance, the HPA process and the dependence of TiN thickness on ferroelectricity demonstrate the potential of strain and strain control for low-temperature ferroelectric applications. Therefore, it can be concluded that to achieve low-temperature ferroelectricity, it is necessary to carefully select ALD process parameters and device structure to produce highly dense and strained films, making the o-phase thermodynamically preferable and easy to crystallize. To fully comprehend and optimize the low-temperature ferroelectric behavior of HfO_2-based materials, it is necessary to address several challenges and unanswered questions. The mechanisms of phase formation and stabilization, the role of defects and interfaces, and the reliability and endurance issues resulting from low-temperature processes are some areas that require further investigation. We hope this review will provide helpful insights and guidance for researchers interested in exploring the fascinating field of nanoscale ferroelectricity.

AUTHOR INFORMATION

Corresponding Authors

*e-mail: sijoon.kim@kangwon.ac.kr and jiyoung.kim@utdallas.edu

Author Contributions

All authors have given approval to the final version of the manuscript.

Notes

Any additional relevant notes should be placed here.

ACKNOWLEDGMENT

We would like to thank Semiconductor Research Cooperation (SRC) for their financial support through GRC-LMD program (task#3001.001) and also RASIRC Inc. for their funding. We also thank YEST for their funding by Technology Innovation Program (No.20010806) from the Korean government (MOTIE) and Korea Institute for Advancement of Technology (KIAT) grant funded by the Korea government (MOTIE) (P0017011 and P0020966, HRD Program for Industrial Innovation). We must also thank Dr. Venkateswarlu Gaddam for his help in preparing this manuscript. This research used beamline 12ID (SMI) of the National Synchrotron Light Source II (NSLS-II) and utilized the X-ray partner user program at the Center for Functional Nanomaterials (CFN), both of which are U.S. Department of Energy (DOE) Office of Science User Facilities operated for the DOE Office of Science by Brookhaven National Laboratory under Contract No. DE-SC0012704.

REFERENCES

(1) Böscke, T. S.; Müller, J.; Bräuhaus, D.; Schröder, U.; Böttger, U. Ferroelectricity in Hafnium Oxide Thin Films. *Appl. Phys. Lett.* **2011**, *99* (10), 102903. DOI: 10.1063/1.3634052.

(2) Huan, T. D.; Sharma, V.; Rossetti, G. A.; Ramprasad, R. Pathways towards Ferroelectricity in Hafnia. *Phys. Rev. B* **2014**, *90* (6), 064111. DOI:

10.1103/PhysRevB.90.064111.

(3) Materlik, R.; Kunneth, C.; Kersch, A. The Origin of Ferroelectricity in $Hf_{1-x}Zr_xO_2$: A Computational Investigation and a Surface Energy Model. *J. Appl. Phys.* **2015**, *117* (13), 134109. DOI: 10.1063/1.4916707.

(4) Chae, K.; Hwang, J.; Chagarov, E.; Kummel, A.; Cho, K. Stability of Ferroelectric and Antiferroelectric Hafnium–Zirconium Oxide Thin Films. *J. Appl. Phys.* **2020**, *128* (5), 054101. DOI: 10.1063/5.0011547.

(5) Park, M. H.; Lee, Y. H.; Kim, H. J.; Kim, Y. J.; Moon, T.; Kim, K. Do; Müller, J.; Kersch, A.; Schroeder, U.; Mikolajick, T.; Hwang, C. S. Ferroelectricity and Antiferroelectricity of Doped Thin HfO_2-Based Films. *Adv. Mater.* **2015**, *27* (11), 1811–1831. DOI: 10.1002/adma.201404531.

(6) Park, M. H.; Lee, Y. H.; Mikolajick, T.; Schroeder, U.; Hwang, C. S. Review and Perspective on Ferroelectric HfO_2-Based Thin Films for Memory Applications. *MRS Commun.* **2018**, *8* (3), 795–808. DOI: 10.1557/mrc.2018.175.

(7) Park, M. H.; Lee, D. H.; Yang, K.; Park, J.-Y.; Yu, G. T.; Park, H. W.; Materano, M.; Mittmann, T.; Lomenzo, P. D.; Mikolajick, T.; Schroeder, U.; Hwang, C. S. Review of Defect Chemistry in Fluorite-Structure Ferroelectrics for Future Electronic Devices. *J. Mater. Chem. C* **2020**, *8* (31), 10526–10550. DOI: 10.1039/D0TC01695K.

(8) Lederer, M.; Lehninger, D.; Ali, T.; Kämpfe, T. Review on the Microstructure of Ferroelectric Hafnium Oxides. *Phys. status solidi – Rapid Res. Lett.* **2022**, *16* (10), 2200168. DOI: 10.1002/pssr.202200168.

(9) Kim, S. J.; Mohan, J.; Lee, J. S.; Kim, H. S.; Lee, J.; Young, C. D.; Colombo, L.; Summerfelt, S. R.; San, T.; Kim, J. Stress-Induced Crystallization of Thin $Hf_{1-X}Zr_XO_2$ Films: The Origin of Enhanced Energy Density with Minimized Energy Loss for Lead-Free Electrostatic Energy Storage Applications. *ACS Appl. Mater. Interfaces* **2019**, *11* (5), 5208–5214. DOI: 10.1021/acsami.8b17211.

(10) Kim, S. J.; Mohan, J.; Summerfelt, S. R.; Kim, J. Ferroelectric $Hf_{0.5}Zr_{0.5}O_2$ Thin Films: A Review of Recent Advances. *JOM* **2019**, *71* (1), 246–255. DOI: 10.1007/s11837-018-3140-5.

(11) Mikolajick, T.; Park, M. H.; Begon-Lours, L.; Slesazeck, S. From Ferroelectric Material Optimization to Neuromorphic Devices. *Adv. Mater.* **2023**, 2206042. DOI: 10.1002/adma.202206042.

(12) Eshita, T.; Wang, W.; Nomura, K.; Nakamura, K.; Saito, H.; Yamaguchi, H.; Mihara, S.; Hikosaka, Y.; Kataoka, Y.; Kojima, M. Development of Highly Reliable Ferroelectric Random Access Memory and Its Internet of Things Applications. *Jpn. J. Appl. Phys.* **2018**, *57* (11S), 11UA01. DOI: 10.7567/JJAP.57.11UA01.

(13) Khan, A. I.; Keshavarzi, A.; Datta, S. The Future of Ferroelectric Field-Effect Transistor Technology. *Nat. Electron.* **2020**, *3* (10), 588–597. DOI: 10.1038/s41928-020-00492-7.

(14) Robertson, J. High Dielectric Constant Gate Oxides for Metal Oxide Si Transistors. *Reports Prog. Phys.* **2006**, *69* (2), 327–396. DOI: 10.1088/0034-4885/69/2/R02.

(15) Cheynet, M. C.; Pokrant, S.; Tichelaar, F. D.; Rouvière, J.-L. Crystal Structure and Band Gap Determination of HfO_2 Thin Films. *J. Appl. Phys.* **2007**, *101* (5), 54101. DOI:

10.1063/1.2697551.

(16) Gaumer, C.; Martinez, E.; Lhostis, S.; Guittet, M.-J.; Gros-Jean, M.; Barnes, J.-P.; Licitra, C.; Rochat, N.; Barrett, N.; Bertin, F.; Chabli, A. Impact of the TiN Electrode Deposition on the HfO_2 Band Gap for Advanced MOSFET Gate Stacks. *Microelectron. Eng.* **2011**, *88* (1), 72–75. DOI: 10.1016/j.mee.2010.08.023.

(17) Ihlefeld, J. F.; Luk, T. S.; Smith, S. W.; Fields, S. S.; Jaszewski, S. T.; Hirt, D. M.; Riffe, W. T.; Bender, S.; Constantin, C.; Ayyasamy, M. V; Balachandran, P. V; Lu, P.; David Henry, M.; Davids, P. S. Compositional Dependence of Linear and Nonlinear Optical Response in Crystalline Hafnium Zirconium Oxide Thin Films. *J. Appl. Phys.* **2020**, *128* (3), 34101. DOI: 10.1063/5.0012175.

(18) Hsain, H. A.; Lee, Y.; Materano, M.; Mittmann, T.; Payne, A.; Mikolajick, T.; Schroeder, U.; Parsons, G. N.; Jones, J. L. Many Routes to Ferroelectric HfO_2: A Review of Current Deposition Methods. *J. Vac. Sci. Technol. A* **2022**, *40* (1), 010803. DOI: 10.1116/6.0001317.

(19) George, S. M. Atomic Layer Deposition: An Overview. *Chem. Rev.* **2010**, *110* (1), 111–131. DOI: 10.1021/cr900056b.

(20) Schroeder, U.; Materano, M.; Mittmann, T.; Lomenzo, P. D.; Mikolajick, T.; Toriumi, A. Recent Progress for Obtaining the Ferroelectric Phase in Hafnium Oxide Based Films: Impact of Oxygen and Zirconium. *Jpn. J. Appl. Phys.* **2019**, *58* (SL), SL0801. DOI: 10.7567/1347-4065/ab45e3.

(21) Wang, X.; Mikolajick, T.; Grube, M. Sputtered Ferroelectric Hafnium–Zirconium Oxide

with High Remanent Polarization after Back-End-of-Line Compatible Annealing. *ACS Appl. Electron. Mater.* **2022**, *4* (12), 6142–6148. DOI: 10.1021/acsaelm.2c01259.

(22) Kim, H. J.; An, Y.; Jung, Y. C.; Mohan, J.; Yoo, J. G.; Kim, Y. I.; Hernandez-Arriaga, H.; Kim, H. S.; Kim, J.; Kim, S. J. Low-Thermal-Budget Fluorite-Structure Ferroelectrics for Future Electronic Device Applications. *Phys. status solidi – Rapid Res. Lett.* **2021**, *15* (5), 2100028. DOI: 10.1002/pssr.202100028.

(23) Müller, J.; Böscke, T. S.; Schröder, U.; Mueller, S.; Bräuhaus, D.; Böttger, U.; Frey, L.; Mikolajick, T. Ferroelectricity in Simple Binary ZrO_2 and HfO_2. *Nano Lett.* **2012**, *12* (8), 4318–4323. DOI: 10.1021/nl302049k.

(24) Kim, S. J.; Narayan, D.; Lee, J.-G.; Mohan, J.; Lee, J. S.; Lee, J.; Kim, H. S.; Byun, Y.-C.; Lucero, A. T.; Young, C. D.; Summerfelt, S. R.; San, T.; Colombo, L.; Kim, J. Large Ferroelectric Polarization of TiN/$Hf_{0.5}Zr_{0.5}O_2$/TiN Capacitors Due to Stress-Induced Crystallization at Low Thermal Budget. *Appl. Phys. Lett.* **2017**, *111* (24), 242901. DOI: 10.1063/1.4995619.

(25) Kim, S. J.; Jung, Y. C.; Mohan, J.; Kim, H. J.; Rho, S. M.; Kim, M. S.; Yoo, J. G.; Park, H. R.; Hernandez-Arriaga, H.; Kim, J.-H.; Kim, H. T.; Choi, D. H.; Jung, J.; Hwang, S. M.; Sejoon Kim, H.; Kim, H. J.; Kim, J. Low-Thermal-Budget (300 °C) Ferroelectric TiN/$Hf_{0.5}Zr_{0.5}O_2$/TiN Capacitors Realized Using High-Pressure Annealing. *Appl. Phys. Lett.* **2021**, *119* (24), 242901. DOI: 10.1063/5.0075466.

(26) Cho, M. K.; Yoo, J. G.; Park, H. R.; Kang, J. M.; Gong, T.; Jung, Y. C.; Kim, J.; Kim, S. J. Furnace Annealing Effect on Ferroelectric $Hf_{0.5}Zr_{0.5}O_2$ Thin Films. *J. Korean Inst. Electr. Electron. Mater. Eng.* **2023**, *36* (1), 88–92. DOI: 10.4313/JKEM.2023.36.1.14.

(27) Lehninger, D.; Mahne, H.; Ali, T.; Hoffmann, R.; Olivo, R.; Lederer, M.; Mertens, K.; Kampfe, T.; Biedermann, K.; Landwehr, M.; Heinig, A.; Wang, D.; Shen, Y.; Bernert, K.; Thiem, S.; Seidel, K. Integration of BEoL Compatible 1T1C FeFET Memory Into an Established CMOS Technology. In *2022 IEEE International Memory Workshop (IMW)*; IEEE, 2022; pp 1–4. DOI: 10.1109/IMW52921.2022.9779252.

(28) Materano, M.; Richter, C.; Mikolajick, T.; Schroeder, U. $Hf_xZr_{1-x}O_2$ Thin Films for Semiconductor Applications: An Hf- and Zr-ALD Precursor Comparison. *J. Vac. Sci. Technol. A* **2020**, *38* (2), 022402. DOI: 10.1116/1.5134135.

(29) Jung, Y. C.; Kim, J.-H.; Hernandez-Arriaga, H.; Mohan, J.; Hwang, S. M.; Le, D. N.; Sahota, A.; Kim, H. S.; Kim, K.; Choi, R.; Nam, C.-Y.; Alvarez, D.; Spiegelman, J.; Kim, S. J.; Kim, J. Robust Low-Temperature (350 °C) Ferroelectric $Hf_{0.5}Zr_{0.5}O_2$ Fabricated Using Anhydrous H_2O_2 as the ALD Oxidant. *Appl. Phys. Lett.* **2022**, *121* (22), 222901. DOI: 10.1063/5.0126695.

(30) Kim, J.-H.; Lee, M.; Lee, S.; Jung, Y. C.; Chor, R.; Kim, H. J.; Kim, S. J.; Kim, J. Strategy for Low Temperature HZO Ferroelectric Capacitors for Back-End of Line Applications. In *2023 7th IEEE Electron Devices Technology & Manufacturing Conference (EDTM)*; IEEE, 2023; pp 1–3. DOI: 10.1109/EDTM55494.2023.10103066.

(31) Cremers, V.; Puurunen, R. L.; Dendooven, J. Conformality in Atomic Layer Deposition: Current Status Overview of Analysis and Modelling. *Appl. Phys. Rev.* **2019**, *6* (2), 021302. DOI: 10.1063/1.5060967.

(32) Oh, I.-K.; Park, B.-E.; Seo, S.; Yeo, B. C.; Tanskanen, J.; Lee, H.-B.-R.; Kim, W.-H.; Kim, H. Comparative Study of the Growth Characteristics and Electrical Properties of

Atomic-Layer-Deposited HfO_2 Films Obtained from Metal Halide and Amide Precursors. *J. Mater. Chem. C* **2018**, *6* (27), 7367–7376. DOI: 10.1039/C8TC01476K.

(33) Oh, I.; Sandoval, T. E.; Liu, T.; Richey, N. E.; Bent, S. F. Role of Precursor Choice on Area-Selective Atomic Layer Deposition. *Chem. Mater.* **2021**, *33* (11), 3926–3935. DOI: 10.1021/acs.chemmater.0c04718.

(34) Johnson, R. W.; Hultqvist, A.; Bent, S. F. A Brief Review of Atomic Layer Deposition: From Fundamentals to Applications. *Mater. Today* **2014**, *17* (5), 236–246. DOI: 10.1016/j.mattod.2014.04.026.

(35) Reinke, M.; Kuzminykh, Y.; Hoffmann, P. Low Temperature Chemical Vapor Deposition Using Atomic Layer Deposition Chemistry. *Chem. Mater.* **2015**, *27* (5), 1604–1611. DOI: 10.1021/cm504216p.

(36) Polakowski, P.; Müller, J. Ferroelectricity in Undoped Hafnium Oxide. *Appl. Phys. Lett.* **2015**, *106* (23), 232905. DOI: 10.1063/1.4922272.

(37) Pal, A.; Narasimhan, V. K.; Weeks, S.; Littau, K.; Pramanik, D.; Chiang, T. Enhancing Ferroelectricity in Dopant-Free Hafnium Oxide. *Appl. Phys. Lett.* **2017**, *110* (2), 022903. DOI: 10.1063/1.4973928.

(38) Materano, M.; Mittmann, T.; Lomenzo, P. D.; Zhou, C.; Jones, J. L.; Falkowski, M.; Kersch, A.; Mikolajick, T.; Schroeder, U. Influence of Oxygen Content on the Structure and Reliability of Ferroelectric $Hf_xZr_{1-x}O_2$ Layers. *ACS Appl. Electron. Mater.* **2020**, *2* (11), 3618–3626. DOI: 10.1021/acsaelm.0c00680.

(39) Kim, K. D.; Park, M. H.; Kim, H. J.; Kim, Y. J.; Moon, T.; Lee, Y. H.; Hyun, S. D.;

Gwon, T.; Hwang, C. S. Ferroelectricity in Undoped-HfO_2 Thin Films Induced by Deposition Temperature Control during Atomic Layer Deposition. *J. Mater. Chem. C* **2016**, *4* (28), 6864–6872. DOI: 10.1039/C6TC02003H.

(40) Batra, R.; Huan, T. D.; Rossetti, G. A.; Ramprasad, R. Dopants Promoting Ferroelectricity in Hafnia: Insights from a Comprehensive Chemical Space Exploration. *Chem. Mater.* **2017**, *29* (21), 9102–9109. DOI: 10.1021/acs.chemmater.7b02835.

(41) Mueller, S.; Mueller, J.; Singh, A.; Riedel, S.; Sundqvist, J.; Schroeder, U.; Mikolajick, T. Incipient Ferroelectricity in Al-Doped HfO_2 Thin Films. *Adv. Funct. Mater.* **2012**, *22* (11), 2412–2417. DOI: 10.1002/adfm.201103119.

(42) Mart, C.; Kühnel, K.; Kämpfe, T.; Czernohorsky, M.; Wiatr, M.; Kolodinski, S.; Weinreich, W. Doping Ferroelectric Hafnium Oxide by In-Situ Precursor Mixing. *ACS Appl. Electron. Mater.* **2019**, *1* (12), 2612–2618. DOI: 10.1021/acsaelm.9b00591.

(43) Lomenzo, P. D.; Takmeel, Q.; Moghaddam, S.; Nishida, T. Annealing Behavior of Ferroelectric Si-Doped HfO_2 Thin Films. *Thin Solid Films* **2016**, *615*, 139–144. DOI: 10.1016/j.tsf.2016.07.009.

(44) Mueller, S.; Muller, J.; Schroeder, U.; Mikolajick, T. Reliability Characteristics of Ferroelectric Si:HfO_2 Thin Films for Memory Applications. *IEEE Trans. Device Mater. Reliab.* **2013**, *13* (1), 93–97. DOI: 10.1109/TDMR.2012.2216269.

(45) Müller, J.; Schröder, U.; Böscke, T. S.; Müller, I.; Böttger, U.; Wilde, L.; Sundqvist, J.; Lemberger, M.; Kücher, P.; Mikolajick, T.; Frey, L. Ferroelectricity in Yttrium-Doped Hafnium Oxide. *J. Appl. Phys.* **2011**, *110* (11), 114113. DOI: 10.1063/1.3667205.

(46) Schroeder, U.; Richter, C.; Park, M. H.; Schenk, T.; Pešić, M.; Hoffmann, M.; Fengler, F. P. G.; Pohl, D.; Rellinghaus, B.; Zhou, C.; Chung, C.-C.; Jones, J. L.; Mikolajick, T. Lanthanum-Doped Hafnium Oxide: A Robust Ferroelectric Material. *Inorg. Chem.* **2018**, *57* (5), 2752–2765. DOI: 10.1021/acs.inorgchem.7b03149.

(47) Hoffmann, M.; Schenk, T.; Kulemanov, I.; Adelmann, C.; Popovici, M.; Schroeder, U.; Mikolajick, T. Low Temperature Compatible Hafnium Oxide Based Ferroelectrics. *Ferroelectrics* **2015**, *480* (1), 16–23. DOI: 10.1080/00150193.2015.1012401.

(48) Schenk, T.; Mueller, S.; Schroeder, U.; Materlik, R.; Kersch, A.; Popovici, M.; Adelmann, C.; Van Elshocht, S.; Mikolajick, T. Strontium Doped Hafnium Oxide Thin Films: Wide Process Window for Ferroelectric Memories. In *2013 Proceedings of the European Solid-State Device Research Conference (ESSDERC)*; IEEE, 2013; pp 260–263. DOI: 10.1109/ESSDERC.2013.6818868.

(49) Liao, J.; Zeng, B.; Sun, Q.; Chen, Q.; Liao, M.; Qiu, C.; Zhang, Z.; Zhou, Y. Grain Size Engineering of Ferroelectric Zr-Doped HfO_2 for the Highly Scaled Devices Applications. *IEEE Electron Device Lett.* **2019**, *40* (11), 1868–1871. DOI: 10.1109/LED.2019.2944491.

(50) Andersen, A.; Persson, A. E. O.; Wernersson, L.-E. As-Deposited Ferroelectric HZO on a III–V Semiconductor. *Appl. Phys. Lett.* **2022**, *121* (1), 012901. DOI: 10.1063/5.0097462.

(51) Athle, R.; Blom, T.; Irish, A.; Persson, A. E. O.; Wernersson, L.; Timm, R.; Borg, M. Improved Endurance of Ferroelectric $Hf_xZr_{1-x}O_2$ Integrated on InAs Using Millisecond Annealing. *Adv. Mater. Interfaces* **2022**, *9* (27), 2201038. DOI: 10.1002/admi.202201038.

(52) Liu, W.-Y.; Liao, J.-J.; Jiang, J.; Zhou, Y.-C.; Chen, Q.; Mo, S.-T.; Yang, Q.; Peng, Q.-X.;

Jiang, L.-M. Highly Stable Performance of Flexible $Hf_{0.6}Zr_{0.4}O_2$ Ferroelectric Thin Films under Multi-Service Conditions. *J. Mater. Chem. C* **2020**, *8* (11), 3878–3886. DOI: 10.1039/C9TC05157K.

(53) Persson, A. E. O.; Athle, R.; Littow, P.; Persson, K.-M.; Svensson, J.; Borg, M.; Wernersson, L.-E. Reduced Annealing Temperature for Ferroelectric HZO on InAs with Enhanced Polarization. *Appl. Phys. Lett.* **2020**, *116* (6), 062902. DOI: 10.1063/1.5141403.

(54) Zarubin, S.; Suvorova, E.; Spiridonov, M.; Negrov, D.; Chernikova, A.; Markeev, A.; Zenkevich, A. Fully ALD-Grown TiN/$Hf_{0.5}Zr_{0.5}O_2$/TiN Stacks: Ferroelectric and Structural Properties. *Appl. Phys. Lett.* **2016**, *109* (19), 192903. DOI: 10.1063/1.4966219.

(55) Oh, S.; Kim, H.; Kashir, A.; Hwang, H. Effect of Dead Layers on the Ferroelectric Property of Ultrathin $HfZrO_x$ Film. *Appl. Phys. Lett.* **2020**, *117* (25), 252906. DOI: 10.1063/5.0030856.

(56) Toprasertpong, K.; Tahara, K.; Hikosaka, Y.; Nakamura, K.; Saito, H.; Takenaka, M.; Takagi, S. Low Operating Voltage, Improved Breakdown Tolerance, and High Endurance in $Hf_{0.5}Zr_{0.5}O_2$ Ferroelectric Capacitors Achieved by Thickness Scaling Down to 4 nm for Embedded Ferroelectric Memory. *ACS Appl. Mater. Interfaces* **2022**, *14* (45), 51137–51148. DOI: 10.1021/acsami.2c15369.

(57) Onaya, T.; Nabatame, T.; Sawamoto, N.; Ohi, A.; Ikeda, N.; Nagata, T.; Ogura, A. Ferroelectricity of $Hf_xZr_{1-x}O_2$ Thin Films Fabricated by 300 °C Low Temperature Process with Plasma-Enhanced Atomic Layer Deposition. *Microelectron. Eng.* **2019**, *215* (April), 111013. DOI: 10.1016/j.mee.2019.111013.

(58) Onaya, T.; Nabatame, T.; Jung, Y. C.; Hernandez-Arriaga, H.; Mohan, J.; Kim, H. S.; Sawamoto, N.; Nam, C.-Y.; Tsai, E. H. R.; Nagata, T.; Kim, J.; Ogura, A. Correlation between Ferroelectricity and Ferroelectric Orthorhombic Phase of $Hf_xZr_{1-x}O_2$ Thin Films Using Synchrotron x-Ray Analysis. *APL Mater.* **2021**, *9* (3), 031111. DOI: 10.1063/5.0035848.

(59) Alcala, R.; Richter, C.; Materano, M.; Lomenzo, P. D.; Zhou, C.; Jones, J. L.; Mikolajick, T.; Schroeder, U. Influence of Oxygen Source on the Ferroelectric Properties of ALD Grown $Hf_{1-x}Zr_xO_2$ Films. *J. Phys. D. Appl. Phys.* **2021**, *54* (3), 035102. DOI: 10.1088/1361-6463/abbc98.

(60) Kim, H.-B.; Jung, M.; Oh, Y.; Lee, S. W.; Suh, D.; Ahn, J.-H. Superior and Stable Ferroelectric Properties of Hafnium-Zirconium-Oxide Thin Films Deposited via Atomic Layer Deposition Using Cyclopentadienyl-Based Precursors without Annealing. *Nanoscale* **2021**, *13* (18), 8524–8530. DOI: 10.1039/D1NR01535D.

(61) Oh, Y.; Kim, H.-B.; Lee, S. W.; Jeong, M. J.; Park, T. J.; Ahn, J.-H. Effects of Zr Content and Annealing on Ferroelectricity of As-Grown Crystalline $Hf_{1-x}Zr_xO_2$ Thin Films Using $Hf[Cp(NMe_2)_3]$ and $Zr[Cp(NMe_2)_3]$ Precursors via Atomic Layer Deposition. *Ceram. Int.* **2022**, *48* (17), 25661–25665. DOI: 10.1016/j.ceramint.2022.05.397.

(62) Lederer, M.; Abdulazhanov, S.; Olivo, R.; Lehninger, D.; Kämpfe, T.; Seidel, K.; Eng, L. M. Electric Field-Induced Crystallization of Ferroelectric Hafnium Zirconium Oxide. *Sci. Rep.* **2021**, *11* (1), 22266. DOI: 10.1038/s41598-021-01724-2.

(63) Lehninger, D.; Ali, T.; Olivo, R.; Lederer, M.; Kampfe, T.; Mertens, K.; Seidel, K. Furnace Annealed HfO_2-Films for the Integration of Ferroelectric Functionalities into the

BEoL. In *2020 Joint Conference of the IEEE International Frequency Control Symposium and International Symposium on Applications of Ferroelectrics (IFCS-ISAF)*; IEEE, 2020; pp 1–3. DOI: 10.1109/IFCS-ISAF41089.2020.9234879.

(64) Kim, B. S.; Hyun, S. D.; Moon, T.; Do Kim, K.; Lee, Y. H.; Park, H. W.; Lee, Y. Bin; Roh, J.; Kim, B. Y.; Kim, H. H.; Park, M. H.; Hwang, C. S. A Comparative Study on the Ferroelectric Performances in Atomic Layer Deposited $Hf_{0.5}Zr_{0.5}O_2$ Thin Films Using Tetrakis(Ethylmethylamino) and Tetrakis(Dimethylamino) Precursors. *Nanoscale Res. Lett.* **2020**, *15* (1), 72. DOI: 10.1186/s11671-020-03301-4.

(65) Walters, G.; Shekhawat, A.; Rudawski, N. G.; Moghaddam, S.; Nishida, T. Tiered Deposition of Sub-5 nm Ferroelectric $Hf_{1-x}Zr_xO_2$ Films on Metal and Semiconductor Substrates. *Appl. Phys. Lett.* **2018**, *112* (19), 192901. DOI: 10.1063/1.5027516.

(66) Chang, T.-J.; Jiang, Y.-S.; Yi, S.-H.; Chou, C.-Y.; Wang, C.-I.; Lin, H.-C.; Chen, M.-J. Atomic Tailoring of Low-Thermal-Budget and Nearly Wake-up-Free Ferroelectric $Hf_{0.5}Zr_{0.5}O_2$ Nanoscale Thin Films by Atomic Layer Annealing. *Appl. Surf. Sci.* **2022**, *591* (March), 153110. DOI: 10.1016/j.apsusc.2022.153110.

(67) Hur, J.; Wang, P.; Tasneem, N.; Wang, Z.; Khan, A. I.; Yu, S. Exploring Argon Plasma Effect on Ferroelectric $Hf_{0.5}Zr_{0.5}O_2$ Thin Film Atomic Layer Deposition. *J. Mater. Res.* **2021**, *36* (5), 1206–1213. DOI: 10.1557/s43578-020-00074-5.

(68) Xiao, W.; Liu, C.; Peng, Y.; Zheng, S.; Feng, Q.; Zhang, C.; Zhang, J.; Hao, Y.; Liao, M.; Zhou, Y. Thermally Stable and Radiation Hard Ferroelectric $Hf_{0.5}Zr_{0.5}O_2$ Thin Films on Muscovite Mica for Flexible Nonvolatile Memory Applications. *ACS Appl. Electron. Mater.* **2019**, *1* (6), 919–927. DOI: 10.1021/acsaelm.9b00107.

(69) Kim, S. J.; Mohan, J.; Kim, H. S.; Lee, J.; Hwang, S. M.; Narayan, D.; Lee, J.-G.; Young, C. D.; Colombo, L.; Goodman, G.; Wan, A. S.; Cha, P.-R.; Summerfelt, S. R.; San, T.; Kim, J. Effect of Hydrogen Derived from Oxygen Source on Low-Temperature Ferroelectric TiN/$Hf_{0.5}Zr_{0.5}O_2$/TiN Capacitors. *Appl. Phys. Lett.* **2019**, *115* (18), 182901. DOI: 10.1063/1.5126144.

(70) Kim, S. J.; Mohan, J.; Kim, H. S.; Lee, J.; Young, C. D.; Colombo, L.; Summerfelt, S. R.; San, T.; Kim, J. Low-Voltage Operation and High Endurance of 5-nm Ferroelectric $Hf_{0.5}Zr_{0.5}O_2$ Capacitors. *Appl. Phys. Lett.* **2018**, *113* (18), 182903. DOI: 10.1063/1.5052012.

(71) More Moore. *Int. Roadmap Devices Syst.* **2020**.

(72) Hsain, H. A.; Lee, Y.; Parsons, G.; Jones, J. L. Compositional Dependence of Crystallization Temperatures and Phase Evolution in Hafnia-Zirconia $(Hf_xZr_{1-x})O_2$ Thin Films. *Appl. Phys. Lett.* **2020**, *116* (19), 192901. DOI: 10.1063/5.0002835.

(73) Hwang, S. M.; Kondusamy, A. L. N.; Qin, Z.; Kim, H. S.; Meng, X.; Kim, J.; Hwang, B. K.; Zhou, X.; Telgenhoff, M.; Young, J. Hollow Cathode Plasma (HCP) Enhanced Atomic Layer Deposition of Silicon Nitride (SiN_x) Thin Films Using Pentachlorodisilane (PCDS). *ECS Trans.* **2019**, *89* (3), 63–69. DOI: 10.1149/08903.0063ecst.

(74) Hwang, S. M.; Kim, H. S.; Le, D. N.; Ravichandran, A. V.; Sahota, A.; Lee, J.; Jung, Y. C.; Kim, S. J.; Ahn, J.; Hwang, B. K.; Lee, L.; Zhou, X.; Kim, J. Plasma-Enhanced Atomic-Layer Deposition of Nanometer-Thick SiN_x Films Using Trichlorodisilane for Etch-Resistant Coatings. *ACS Appl. Nano Mater.* **2021**, *4* (3), 2558–2564. DOI: 10.1021/acsanm.0c03203.

(75) Lehninger, D.; Olivo, R.; Ali, T.; Lederer, M.; Kämpfe, T.; Mart, C.; Biedermann, K.; Kühnel, K.; Roy, L.; Kalkani, M.; Seidel, K. Back-End-of-Line Compatible Low-Temperature Furnace Anneal for Ferroelectric Hafnium Zirconium Oxide Formation. *Phys. status solidi* **2020**, *217* (8), 1900840. DOI: 10.1002/pssa.201900840.

(76) Ngoc Van, T. T.; Jang, D.; Jung, E.; Noh, H.; Moon, J.; Kil, D.-S.; Chung, S.-W.; Shong, B. Role of Cyclopentadienyl Ligands of Group 4 Precursors toward High-Temperature Atomic Layer Deposition. *J. Phys. Chem. C* **2022**, *126* (42), 18090–18099. DOI: 10.1021/acs.jpcc.2c04425.

(77) Chan Won, D.; Rhee, S.-W. Effect of Process Temperature on the Structural and Electrical Properties of Atomic Layer Deposited ZrO_2 Films Using Tris(Dimethylamino) Cyclopentadienyl Zirconium Precursor. *J. Vac. Sci. Technol. B, Nanotechnol. Microelectron. Mater. Process. Meas. Phenom.* **2014**, *32* (3), 03D102. DOI: 10.1116/1.4825109.

(78) An, J.-K.; Kim, J.-T.; Kang, G.; Oh, N. K.; Hahm, S.-H.; Lee, G.; Park, I.-S.; Yun, J.-Y. ZrO_2 Film Prepared by Atomic Layer Deposition Using Less Viscous Cocktail $CpZr[N(CH_3)_2]_3/C_7H_8$ Precursor and Ozone. *J. Alloys Compd.* **2017**, *701*, 310–315. DOI: 10.1016/j.jallcom.2016.12.420.

(79) Meng, X.; Byun, Y.-C.; Kim, H.; Lee, J.; Lucero, A.; Cheng, L.; Kim, J. Atomic Layer Deposition of Silicon Nitride Thin Films: A Review of Recent Progress, Challenges, and Outlooks. *Materials (Basel).* **2016**, *9* (12), 1007. DOI: 10.3390/ma9121007.

(80) Knoops, H. C. M.; Faraz, T.; Arts, K.; Kessels, W. M. M. (Erwin). Status and Prospects of Plasma-Assisted Atomic Layer Deposition. *J. Vac. Sci. Technol. A* **2019**, *37* (3), 030902.

DOI: 10.1116/1.5088582.

(81) Ha, S.-C.; Choi, E.; Kim, S.-H.; Sung Roh, J. Influence of Oxidant Source on the Property of Atomic Layer Deposited Al_2O_3 on Hydrogen-Terminated Si Substrate. *Thin Solid Films* **2005**, *476* (2), 252–257. DOI: 10.1016/j.tsf.2004.09.035.

(82) Hsain, H. A.; Lee, Y.; Lancaster, S.; Materano, M.; Alcala, R.; Xu, B.; Mikolajick, T.; Schroeder, U.; Parsons, G. N.; Jones, J. L. Role of Oxygen Source on Buried Interfaces in Atomic-Layer-Deposited Ferroelectric Hafnia–Zirconia Thin Films. *ACS Appl. Mater. Interfaces* **2022**, *14* (37), 42232–42244. DOI: 10.1021/acsami.2c11073.

(83) Park, H. B.; Cho, M.; Park, J.; Lee, S. W.; Hwang, C. S.; Kim, J.-P.; Lee, J.-H.; Lee, N.-I.; Kang, H.-K.; Lee, J.-C.; Oh, S.-J. Comparison of HfO_2 Films Grown by Atomic Layer Deposition Using $HfCl_4$ and H_2O or O_3 as the Oxidant. *J. Appl. Phys.* **2003**, *94* (5), 3641–3647. DOI: 10.1063/1.1599980.

(84) Cho, M.; Jeong, D. S.; Park, J.; Park, H. B.; Lee, S. W.; Park, T. J.; Hwang, C. S.; Jang, G. H.; Jeong, J. Comparison between Atomic-Layer-Deposited HfO_2 Films Using O_3 or H_2O Oxidant and $Hf[N(CH_3)_2]_4$ Precursor. *Appl. Phys. Lett.* **2004**, *85* (24), 5953–5955. DOI: 10.1063/1.1829773.

(85) Liu, X.; Ramanathan, S.; Longdergan, A.; Srivastava, A.; Lee, E.; Seidel, T. E.; Barton, J. T.; Pang, D.; Gordon, R. G. ALD of Hafnium Oxide Thin Films from Tetrakis(Ethylmethylamino)Hafnium and Ozone. *J. Electrochem. Soc.* **2005**, *152* (3), G213. DOI: 10.1149/1.1859631.

(86) Choi, M.-J.; Park, H.-H.; Jeong, D. S.; Kim, J. H.; Kim, J.-S.; Kim, S. K. Atomic Layer

Deposition of HfO_2 Thin Films Using H_2O_2 as Oxidant. *Appl. Surf. Sci.* **2014**, *301*, 451–455. DOI: 10.1016/j.apsusc.2014.02.098.

(87) *National Bureau of Standards, National Standard Reference Data Series*; National Institute of Standards and Technology, 1970.

(88) Rezaei, F.; Vanraes, P.; Nikiforov, A.; Morent, R.; De Geyter, N. Applications of Plasma-Liquid Systems: A Review. *Materials (Basel).* **2019**, *12* (17), 2751. DOI: 10.3390/ma12172751.

(89) Spiegelman, J.; Alvarez, D. Cheating Raoult's Law to Enable Delivery of Hydrogen Peroxide as a Stable Vapor. *Gases Instrum.* **2015**, 14–19.

(90) Giguère, P. A.; Maass, O. VAPOUR PRESSURES AND BOILING POINTS OF BINARY MIXTURES OF HYDROGEN PEROXIDE AND WATER. *Can. J. Res.* **1940**, *18b* (7), 181–193. DOI: 10.1139/cjr40b-023.

(91) Scatchard, G.; Kavanagh, G. M.; Ticknor, L. B. Vapor-Liquid Equilibrium. VIII. Hydrogen Peroxide—Water Mixtures. *J. Am. Chem. Soc.* **1952**, *74* (15), 3715–3720. DOI: 10.1021/ja01135a001.

(92) Xiao, D.-Q.; Luo, B.-B.; Xiong, W.; Wu, X.; Zhang, D. W.; Ding, S.-J. Low Thermal Budget Fabrication and Performance Comparison of MFM Capacitors With Thermal and Plasma-Enhanced Atomic Layer Deposited $Hf_{0.45}Zr_{0.55}O_2$ Ferroelectrics. *IEEE Trans. Electron Devices* **2021**, *68* (12), 6359–6364. DOI: 10.1109/TED.2021.3118665.

(93) Hamouda, W.; Lubin, C.; Ueda, S.; Yamashita, Y.; Renault, O.; Mehmood, F.; Mikolajick, T.; Schroeder, U.; Negrea, R.; Barrett, N. Interface Chemistry of Pristine

TiN/La:$Hf_{0.5}Zr_{0.5}O_2$ Capacitors. *Appl. Phys. Lett.* **2020**, *116* (25), 252903. DOI: 10.1063/5.0012595.

(94) Calka, P.; Sowinska, M.; Bertaud, T.; Walczyk, D.; Dabrowski, J.; Zaumseil, P.; Walczyk, C.; Gloskovskii, A.; Cartoixà, X.; Suñé, J.; Schroeder, T. Engineering of the Chemical Reactivity of the Ti/HfO_2 Interface for RRAM: Experiment and Theory. *ACS Appl. Mater. Interfaces* **2014**, *6* (7), 5056–5060. DOI: 10.1021/am500137y.

(95) Park, M. H.; Kim, H. J.; Kim, Y. J.; Jeon, W.; Moon, T.; Hwang, C. S. Ferroelectric Properties and Switching Endurance of $Hf_{0.5}Zr_{0.5}O_2$ Films on TiN Bottom and TiN or RuO_2 Top Electrodes. *Phys. Status Solidi - Rapid Res. Lett.* **2014**, *8* (6), 532–535. DOI: 10.1002/pssr.201409017.

(96) Pantisano, L.; Afanas'ev, V. V.; Cimino, S.; Adelmann, C.; Goux, L.; Chen, Y. Y.; Kittl, J. A.; Wouters, D.; Jurczak, M. Towards Barrier Height Modulation in HfO_2/TiN by Oxygen Scavenging – Dielectric Defects or Metal Induced Gap States? *Microelectron. Eng.* **2011**, *88* (7), 1251–1254. DOI: 10.1016/j.mee.2011.03.057.

(97) Wu, L.; Yu, H. Y.; Li, X.; Pey, K. L.; Pan, J. S.; Chai, J. W.; Chiu, Y. S.; Lin, C. T.; Xu, J. H.; Wann, H. J.; Yu, X. F.; Lee, D. Y.; Hsu, K. Y.; Tao, H. J. Thermal Stability of TiN Metal Gate Prepared by Atomic Layer Deposition or Physical Vapor Deposition on HfO_2 High-K Dielectric. *Appl. Phys. Lett.* **2010**, *96* (11), 113510. DOI: 10.1063/1.3365241.

(98) Kim, H.; McIntyre, P. C.; On Chui, C.; Saraswat, K. C.; Stemmer, S. Engineering Chemically Abrupt High-k Metal Oxide⁄silicon Interfaces Using an Oxygen-Gettering Metal Overlayer. *J. Appl. Phys.* **2004**, *96* (6), 3467–3472. DOI: 10.1063/1.1776636.

(99) Pešić, M.; Fengler, F. P. G.; Larcher, L.; Padovani, A.; Schenk, T.; Grimley, E. D.; Sang, X.; LeBeau, J. M.; Slesazeck, S.; Schroeder, U.; Mikolajick, T. Physical Mechanisms behind the Field-Cycling Behavior of HfO_2-Based Ferroelectric Capacitors. *Adv. Funct. Mater.* **2016**, *26* (25), 4601–4612. DOI: 10.1002/adfm.201600590.

(100) Islamov, D. R.; Gritsenko, V. A.; Perevalov, T. V; Pustovarov, V. A.; Orlov, O. M.; Chernikova, A. G.; Markeev, A. M.; Slesazeck, S.; Schroeder, U.; Mikolajick, T.; Krasnikov, G. Y. Identification of the Nature of Traps Involved in the Field Cycling of $Hf_{0.5}Zr_{0.5}O_2$-Based Ferroelectric Thin Films. *Acta Mater.* **2019**, *166*, 47–55. DOI: 10.1016/j.actamat.2018.12.008.

(101) Onaya, T.; Nabatame, T.; Sawamoto, N.; Ohi, A.; Ikeda, N.; Chikyow, T.; Ogura, A. Improvement in Ferroelectricity of $Hf_xZr_{1-x}O_2$ Thin Films Using ZrO_2 Seed Layer. *Appl. Phys. Express* **2017**, *10* (8), 081501. DOI: 10.7567/APEX.10.081501.

(102) Onaya, T.; Nabatame, T.; Inoue, M.; Jung, Y. C.; Hernandez-Arriaga, H.; Mohan, J.; Kim, H. S.; Sawamoto, N.; Nagata, T.; Kim, J.; Ogura, A. Improvement in Ferroelectricity and Breakdown Voltage of over 20-nm-Thick $Hf_xZr_{1-x}O_2/ZrO_2$ Bilayer by Atomic Layer Deposition. *Appl. Phys. Lett.* **2020**, *117* (23), 232902. DOI: 10.1063/5.0029709.

(103) Onaya, T.; Nabatame, T.; Sawamoto, N.; Ohi, A.; Ikeda, N.; Nagata, T.; Ogura, A. Improvement in Ferroelectricity of $Hf_xZr_{1-x}O_2$ Thin Films Using Top- and Bottom-ZrO_2 Nucleation Layers. *APL Mater.* **2019**, *7* (6), 061107. DOI: 10.1063/1.5096626.

(104) Lovesey, S. W. *Theory of Neutron Scattering from Condensed Matter*; Oxford Science Publications, Clarendon Press, 1984.

(105) Abeykoon, S. K.; Zhang, Y.; Dill, E. D.; Caswell, T. A.; Allan, D. B.; Akilic, A.; Wiegart, L.; Wilkins, S.; Heroux, A.; van Dam, K. K.; Sutton, M.; Fluerasu, A. Software Tools for X-Ray Photon Correlation and X-Ray Speckle Visibility Spectroscopy. In *2016 New York Scientific Data Summit (NYSDS)*; IEEE, 2016; pp 1–10. DOI: 10.1109/NYSDS.2016.7747815.

(106) Kim, S. J.; Mohan, J.; Lee, J.; Lee, J. S.; Lucero, A. T.; Young, C. D.; Colombo, L.; Summerfelt, S. R.; San, T.; Kim, J. Effect of Film Thickness on the Ferroelectric and Dielectric Properties of Low-Temperature (400 °C) $Hf_{0.5}Zr_{0.5}O_2$ Films. *Appl. Phys. Lett.* **2018**, *112* (17), 172902. DOI: 10.1063/1.5026715.

(107) O'Connor, É.; Halter, M.; Eltes, F.; Sousa, M.; Kellock, A.; Abel, S.; Fompeyrine, J. Stabilization of Ferroelectric $Hf_xZr_{1-x}O_2$ Films Using a Millisecond Flash Lamp Annealing Technique. *APL Mater.* **2018**, *6* (12), 121103. DOI: 10.1063/1.5060676.

(108) Chen, K.-Y.; Chen, P.-H.; Kao, R.-W.; Lin, Y.-X.; Wu, Y.-H. Impact of Plasma Treatment on Reliability Performance for $HfZrO_x$-Based Metal-Ferroelectric-Metal Capacitors. *IEEE Electron Device Lett.* **2018**, *39* (1), 87–90. DOI: 10.1109/LED.2017.2771390.

(109) Mittmann, T.; Fengler, F. P. G.; Richter, C.; Park, M. H.; Mikolajick, T.; Schroeder, U. Optimizing Process Conditions for Improved $Hf_{1-x}Zr_xO_2$ Ferroelectric Capacitor Performance. *Microelectron. Eng.* **2017**, *178*, 48–51. DOI: 10.1016/j.mee.2017.04.031.

(110) Fields, S. S.; Smith, S. W.; Ryan, P. J.; Jaszewski, S. T.; Brummel, I. A.; Salanova, A.; Esteves, G.; Wolfley, S. L.; Henry, M. D.; Davids, P. S.; Ihlefeld, J. F. Phase-Exchange-Driven Wake-Up and Fatigue in Ferroelectric Hafnium Zirconium Oxide Films. *ACS Appl. Mater. Interfaces* **2020**, *12* (23), 26577–26585. DOI: 10.1021/acsami.0c03570.

(111) Grimley, E. D.; Schenk, T.; Sang, X.; Pešić, M.; Schroeder, U.; Mikolajick, T.; LeBeau, J. M. Structural Changes Underlying Field-Cycling Phenomena in Ferroelectric HfO_2 Thin Films. *Adv. Electron. Mater.* **2016**, *2* (9), 1600173. DOI: 10.1002/aelm.201600173.

(112) Hoffmann, M.; Schroeder, U.; Schenk, T.; Shimizu, T.; Funakubo, H.; Sakata, O.; Pohl, D.; Drescher, M.; Adelmann, C.; Materlik, R.; Kersch, A.; Mikolajick, T. Stabilizing the Ferroelectric Phase in Doped Hafnium Oxide. *J. Appl. Phys.* **2015**, *118* (7), 072006. DOI: 10.1063/1.4927805.

(113) Toprasertpong, K.; Tahara, K.; Fukui, T.; Lin, Z.; Watanabe, K.; Takenaka, M.; Takagi, S. Improved Ferroelectric/Semiconductor Interface Properties in $Hf_{0.5}Zr_{0.5}O_2$ Ferroelectric FETs by Low-Temperature Annealing. *IEEE Electron Device Lett.* **2020**, *41* (10), 1588–1591. DOI: 10.1109/LED.2020.3019265.

(114) Onaya, T.; Nabatame, T.; Inoue, M.; Sawada, T.; Ota, H.; Morita, Y. Study of SiO_2 Interfacial Layer Growth during Fabrication Process of Ferroelectric $Hf_xZr_{1-x}O_2$ -Based Metal-Ferroelectric Semiconductor. *ECS Trans.* **2021**, *104* (4), 129–135. DOI: 10.1149/10404.0129ecst.

(115) Muller, J.; Polakowski, P.; Muller, S.; Mulaosmanovic, H.; Ocker, J.; Mikolajick, T.; Slesazeck, S.; Muller, S.; Ocker, J.; Mikolajick, T.; Flachowsky, S.; Trentzsch, M. High Endurance Strategies for Hafnium Oxide Based Ferroelectric Field Effect Transistor. In *2016 16th Non-Volatile Memory Technology Symposium (NVMTS)*; IEEE, 2016; pp 1–7. DOI: 10.1109/NVMTS.2016.7781517.

(116) Pesic, M.; Beltrando, B.; Padovani, A.; Gangopadhyay, S.; Kaliappan, M.; Haverty, M.; Villena, M. A.; Piccinini, E.; Bertocchi, M.; Chiang, T.; Larcher, L.; Strand, J.; Shluger,

A. L. Variability Sources and Reliability of 3D — FeFETs. In *2021 IEEE International Reliability Physics Symposium (IRPS)*; IEEE, 2021; Vol. 2021-March, pp 1–7. DOI: 10.1109/IRPS46558.2021.9405118.

(117) Hernandez-Arriaga, H.; Mohan, J.; Jung, Y. C.; Kim, J.-H.; Rho, C.-H.; Choi, R.; Kim, J. Evaluation of the O_3 and H_2O Oxidants in Downscaling Eot of Ferroelectric $Hf_{0.5}Zr_{0.5}O_2$ on Silicon. *ECS Meet. Abstr.* **2022**, *MA2022-01* (19), 1074–1074. DOI: 10.1149/MA2022-01191074mtgabs.

(118) Sk, M. R.; Thunder, S.; Lehninger, D.; Sanctis, S.; Raffel, Y.; Lederer, M.; Jank, M. P. M.; Kämpfe, T.; De, S.; Chakrabarti, B. Ferroelectric Content-Addressable Memory Cells with IGZO Channel: Impact of Retention Degradation on the Multibit Operation. *ACS Appl. Electron. Mater.* **2023**, *5* (2), 812–820. DOI: 10.1021/acsaelm.2c01357.

(119) Dutta, S.; Ye, H.; Chakraborty, W.; Luo, Y.-C.; Jose, M. S.; Grisafe, B.; Khanna, A.; Lightcap, I.; Shinde, S.; Yu, S.; Datta, S. Monolithic 3D Integration of High Endurance Multi-Bit Ferroelectric FET for Accelerating Compute-In-Memory. In *2020 IEEE International Electron Devices Meeting (IEDM)*; IEEE, 2020; Vol. 2020-Decem, pp 36.4.1-36.4.4. DOI: 10.1109/IEDM13553.2020.9371974.

(120) Lehninger, D.; Ellinger, M.; Ali, T.; Li, S.; Mertens, K.; Lederer, M.; Olivio, R.; Kämpfe, T.; Hanisch, N.; Biedermann, K.; Rudolph, M.; Brackmann, V.; Sanctis, S.; Jank, M. P. M.; Seidel, K. A Fully Integrated Ferroelectric Thin-Film-Transistor – Influence of Device Scaling on Threshold Voltage Compensation in Displays. *Adv. Electron. Mater.* **2021**, *7* (6), 2100082. DOI: 10.1002/aelm.202100082.

(121) Onaya, T.; Nabatame, T.; Inoue, M.; Sawada, T.; Ota, H.; Morita, Y. Wake-up-Free

Properties and High Fatigue Resistance of $Hf_xZr_{1-x}O_2$-Based Metal–Ferroelectric–Semiconductor Using Top ZrO_2 Nucleation Layer at Low Thermal Budget (300 °C). *APL Mater.* **2022**, *10* (5), 051110. DOI: 10.1063/5.0091661.

(122) Onaya, T.; Nabatame, T.; Inoue, M.; Jung, Y. C.; Hernandez-Arriaga, H.; Mohan, J.; Kim, H. S.; Sawamoto, N.; Nagata, T.; Kim, J.; Ogura, A. Improvement of Ferroelectricity and Fatigue Property of Thicker $Hf_xZr_{1-x}O_2$/ZrO_2 Bi-Layer. *ECS Trans.* **2020**, *98* (3), 63–70. DOI: 10.1149/09803.0063ecst.

(123) Onaya, T.; Nabatame, T.; Sawamoto, N.; Kurishima, K.; Ohi, A.; Ikeda, N.; Nagata, T.; Ogura, A. Ferroelectricity of $Hf_xZr_{1-x}O_2$ Thin Films Fabricated Using TiN Stressor and ZrO_2 Nucleation Techniques. *ECS Trans.* **2018**, *86* (6), 31–38. DOI: 10.1149/08606.0031ecst.

(124) Onaya, T.; Nabatame, T.; Sawada, T.; Kurishima, K.; Sawamoto, N.; Ohi, A.; Chikyow, T.; Ogura, A. Improved Leakage Current Properties of ZrO_2/(Ta/Nb)O_x-Al_2O_3/ZrO_2 Nanolaminate Insulating Stacks for Dynamic Random Access Memory Capacitors. *Thin Solid Films* **2018**, *655* (December 2016), 48–53. DOI: 10.1016/j.tsf.2018.02.010.

(125) Mohan, J.; Hernandez-Arriaga, H.; Jung, Y. C.; Onaya, T.; Nam, C.-Y.; Tsai, E. H. R.; Kim, S. J.; Kim, J. Ferroelectric Polarization Retention with Scaling of $Hf_{0.5}Zr_{0.5}O_2$ on Silicon. *Appl. Phys. Lett.* **2021**, *118* (10), 102903. DOI: 10.1063/5.0035579.

(126) Sun, N.; Zhou, D.; Liu, W.; Zhang, Y.; Li, S.; Wang, J.; Ali, F. Importance of Tailoring the Thickness of SiO_2 Interlayer in the Observation of Ferroelectric Characteristics in Yttrium Doped HfO_2 Films on Silicon. *Vacuum* **2021**, *183* (February 2020), 109835. DOI: 10.1016/j.vacuum.2020.109835.

(127) Morita, Y.; Migita, S.; Mizubayashi, W.; Ota, H. Fabrication of Direct-Contact Higher-k HfO_2 Gate Stacks by Oxygen-Controlled Cap Post-Deposition Annealing. *Jpn. J. Appl. Phys.* **2011**, *50* (10 PART 2). DOI: 10.1143/JJAP.50.10PG01.

(128) Kim, J.; Kim, S.; Jeon, H.; Cho, M.-H.; Chung, K.-B.; Bae, C. Characteristics of HfO_2 Thin Films Grown by Plasma Atomic Layer Deposition. *Appl. Phys. Lett.* **2005**, *87* (5), 053108. DOI: 10.1063/1.2005370.

(129) Florent, K.; Lavizzari, S.; Di Piazza, L.; Popovici, M.; Duan, J.; Groeseneken, G.; Van Houdt, J. Reliability Study of Ferroelectric Al:HfO_2 Thin Films for DRAM and NAND Applications. *IEEE Trans. Electron Devices* **2017**, *64* (10), 4091–4098. DOI: 10.1109/TED.2017.2742549.

(130) Hsu, T.; Kuo, C.; Lin, B.; Shieh, J.; Chen, M.-J. The Effects of Annealing and Wake-up Cycling on the Ferroelectricity of Zirconium Hafnium Oxide Ultrathin Films Prepared by Remote Plasma Atomic Layer Deposition. *Smart Mater. Struct.* **2019**, *28* (8), 084005. DOI: 10.1088/1361-665X/ab23c3.

(131) Künneth, C.; Materlik, R.; Kersch, A. Modeling Ferroelectric Film Properties and Size Effects from Tetragonal Interlayer in $Hf_{1-x}Zr_xO_2$ Grains. *J. Appl. Phys.* **2017**, *121* (20), 205304. DOI: 10.1063/1.4983811.

(132) Kim, S. J.; Mohan, J.; Kim, H. S.; Hwang, S. M.; Kim, N.; Jung, Y. C.; Sahota, A.; Kim, K.; Yu, H.-Y.; Cha, P.-R.; Young, C. D.; Choi, R.; Ahn, J.; Kim, J. A Comprehensive Study on the Effect of TiN Top and Bottom Electrodes on Atomic Layer Deposited Ferroelectric $Hf_{0.5}Zr_{0.5}O_2$ Thin Films. *Materials (Basel).* **2020**, *13* (13), 2968. DOI: 10.3390/ma13132968.

(133) Hamouda, W.; Pancotti, A.; Lubin, C.; Tortech, L.; Richter, C.; Mikolajick, T.; Schroeder, U.; Barrett, N. Physical Chemistry of the TiN/$Hf_{0.5}Zr_{0.5}O_2$ Interface. *J. Appl. Phys.* **2020**, *127* (6), 064105. DOI: 10.1063/1.5128502.

(134) Ando, T. Ultimate Scaling of High-κ Gate Dielectrics: Higher-κ or Interfacial Layer Scavenging? *Materials (Basel).* **2012**, *5* (12), 478–500. DOI: 10.3390/ma5030478.

(135) Starschich, S.; Menzel, S.; Böttger, U. Evidence for Oxygen Vacancies Movement during Wake-up in Ferroelectric Hafnium Oxide. *Appl. Phys. Lett.* **2016**, *108* (3), 032903. DOI: 10.1063/1.4940370.

(136) Huang, C.; Zhang, Y.; Zheng, S.; Yang, Q.; Liao, M. Interface Effects Induced by a ZrO_2 Seed Layer on the Phase Stability and Orientation of HfO_2 Ferroelectric Thin Films: A First-Principles Study. *Phys. Rev. Appl.* **2021**, *16* (4), 044048. DOI: 10.1103/PhysRevApplied.16.044048.

(137) Fields, S. S.; Cai, T.; Jaszewski, S. T.; Salanova, A.; Mimura, T.; Heinrich, H. H.; Henry, M. D.; Kelley, K. P.; Sheldon, B. W.; Ihlefeld, J. F. Origin of Ferroelectric Phase Stabilization via the Clamping Effect in Ferroelectric Hafnium Zirconium Oxide Thin Films. *Adv. Electron. Mater.* **2022**, *8* (12), 2200601. DOI: 10.1002/aelm.202200601.

(138) Park, H. R.; Yoo, J. G.; Kang, J. M.; Cho, M. K.; Gong, T.; Park, S.; Lee, S.; Kim, J.-Hy.; Lee, S.; Choi, R.; Kim, H. S.; Jung, Y. C.; Kim, J.; Kim, S. J. A Study on the Thermal Budget of Ferroelectric TiN/$Hf_{0.5}Zr_{0.5}O_2$/TiN Capacitors for Next-Generation Memory Applications. In *2023 7th IEEE Electron Devices Technology & Manufacturing Conference (EDTM)*; IEEE, 2023; pp 1–3. DOI: 10.1109/EDTM55494.2023.10103015.

(139) Kim, T.; Park, J.; Cheong, B.-H.; Jeon, S. Effects of High Pressure Nitrogen Annealing on Ferroelectric $Hf_{0.5}Zr_{0.5}O_2$ Films. *Appl. Phys. Lett.* **2018**, *112* (9), 092906. DOI: 10.1063/1.5003369.

(140) Kim, H.; Kashir, A.; Oh, S.; Jang, H.; Hwang, H. Effects of High Pressure Oxygen Annealing on $Hf_{0.5}Zr_{0.5}O_2$ Ferroelectric Device. *Nanotechnology* **2021**, *32* (31), 315712. DOI: 10.1088/1361-6528/abfb9a.

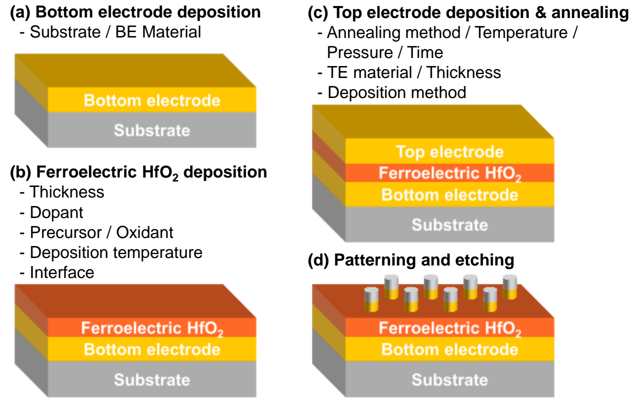

Figure 1. Schematic of the fabrication process for ferroelectric HfO_2-based metal-ferroelectric-metal capacitors. The fabrication process involves (a) bottom electrode deposition, (b) HfO_2-based material deposition, (c) top electrode deposition and annealing to crystalize the HfO_2-based material for ferroelectricity, and (d) patterning and etching to define the capacitor structure. Each step of the fabrication process is accompanied by process parameters and conditions that can affect the ferroelectric properties of the HfO_2-based material.

Table 1. Process parameters of atomic layer deposition and ferroelectric capacitor performance from previous reports.

Material	Thickness (nm)	Doping (%)	Hafnium precursor	Dopant precursor	Oxygen source	Dep.[a] Temp.[b] (°C)	Anneal method	Anneal Temp. (°C)	Anneal time (s)	TE[c]	t_{TE}[d] (nm)	BE[e]	t_{BE} (nm)	$2P_r$ (μC/cm^2)	E_c (MV/cm)	Endurance (cycle)
HfO_2	6	0	$HfCl_4$	N/A[f]	H_2O	300	RTA	650	N/A	TiN	10	TiN	10	20	1	$1.6x10^5$ at 2.5MV/cm, 10kHz[36]
HfO_2	8.3	0	TDMA-Hf	N/A	O_3	260	RTA	650	N/A	TiN	5	TiN	5	27	1	N/A[37]
HfO_2	10	0	TEMA-Hf	N/A	O_3	230	RTA	600	20	TiN	10	Si		22	N/A	N/A[38]
HfO_2	9	0	TEMA-Hf	N/A	O_3	220	RTA	650	30	TiN	5	TiN	50	21	1	10^8 at 3.2MV/cm, 100kHz[39]
$Al:HfO_2$	16	7.1	TEMA-Hf	TMA	O_3	300	RTA	1000	20	TiN	20	TiN	12	12	1	N/A[41]
$Al:HfO_2$	10	2.2	TEMA-Hf	TMA	O_3	280	RTA	650	20	TiN	10	TiN	10	34	0.8	N/A[42]
$Si:HfO_2$	10	4.2	TDMA-Hf	3DMAS	O_2 plasma	200	RTA	900	20	TiN	10	TiN	10	33	1.8	N/A[43]
$Si:HfO_2$	10	2.8	TEMA-Hf	3DMAS	O_3	280	RTA	650	20	TiN	10	TiN	10	38	0.9	N/A[42]
$Si:HfO_2$	10	4.6	TEMA-Hf	4DMAS	O_3	266	RTA	650	20	TiN	10	TiN	10	16	1	10^{10} at 2MV/cm[44]
$Y:HfO_2$	10	5.2	TEMA-Hf	$Y(MeCp)_3$	O_3	N/A	RTA	600	20	TiN	4	TiN	18	48	1.2	N/A[45]
$La:HfO_2$	10	6	TEMA-Hf	$La(iPrCp)_3$	O_3	280	RTA	650	20	TiN	10	TiN	10	48	1.1	N/A[42]
$La:HfO_2$	12	9.2	TEMA-Hf	$La(iPrCp)_3$	H_2O	280	RTA	800	20	TiN	12	TiN	12	56	1.8	$3x10^5$ at 4MV/cm, 100kHz[46]
$Sr:HfO_2$	10	4.4	$HfCl_4$	$Sr(tBu_3Cp)_2$	H_2O	300	RTA	800	20	TiN	10	TiN	10	30	1.9	10^5 at 4MV/cm, 10kHz[47]
$Sr:HfO_2$	10	9.9	$HfCl_4$	$Sr(tBu_3Cp)_2$	H_2O	300	RTA	800	20	TiN	12	TiN	10	46	1.8	10^6 at 3MV/cm[48]
$Gd:HfO_2$	10	3.4	$HfCl_4$	$Gd(iPrCp)_3$	H_2O	300	RTA	450	600	TiN	10	TiN	10	30	1.6	$2x10^5$ at 4MV/cm, 10kHz[47]
$Zr:HfO_2$	10	50	TDMA-Hf	TDMA-Zr	O_3	260	RTA	450	N/A	TiN	50	TiN	50	51	1	10^9 at 2.5MV/cm, 100kHz[64]
$Zr:HfO_2$	3.7	50	TDMA-Hf	TDMA-Zr	H_2O	175	RTA	500	20	TiN	10	Ir	20	26	1	10^6 at 5.3MV/cm, 100kHz[65]
$Zr:HfO_2$	7	50	TDMA-Hf	TDMA-Zr	H_2O	300	None			TiN	40	Pt	64	6.8	1	N/A[66]
$Zr:HfO_2$	7	50	TDMA-Hf	TDMA-Zr	H_2O	300	ALA			TiN	40	Pt	64	42.6	1	N/A[66]
$Zr:HfO_2$	10	50	TDMA-Hf	TDMA-Zr	H_2O	250	RTA	450	30	TiN	12	TiN	12	26	1	10^7 at 2.5MV/cm[67]
$Zr:HfO_2$	18	50	TDMA-Hf	TDMA-Zr	H_2O	N/A	RTA	500	30	TaN	100	TaN	100	22	1	10^6 at 2.2MV/cm, 100kHz[68]
$Zr:HfO_2$	10	50	TDMA-Hf	TDMA-Zr	H_2O_2	250	RTA	350	60	TiN	90	TiN	90	55	1	10^{10} at 2.0MV/cm, 1MHz[29]
$Zr:HfO_2$	10	50	TDMA-Hf	TDMA-Zr	O_3	250	RTA	400	60	TiN	90	TiN	90	47.3	1	10^7 at 2MV/cm, 33kHz[69]

Table 1. Continued.

Material	Thickness (nm)	Doping (%)	Hafnium precursor	Dopant precursor	Oxygen source	Dep.[a] Temp.[b] (°C)	Anneal method	Anneal Temp. (°C)	Anneal time (s)	TE[c]	t_{TE}[d] (nm)	BE[e]	t_{BE} (nm)	$2P_r$ (μC/cm²)	E_c (MV/cm)	Endurance (cycle)
Zr:HfO_2	10	50	TDMA-Hf	TDMA-Zr	H_2O	250	RTA	400	60	TiN	90	TiN	90	38.7	1	10^7 at 2MV/cm, 33kHz[69]
Zr:HfO_2	5	50	TDMA-Hf	TDMA-Zr	O_3	250	RTA	450	60	TiN	90	TiN	90	20	1	>10^{10} at 2.4MV/cm, 33kHz[70]
Zr:HfO_2	10	50	TDMA-Hf	TDMA-Zr	O_3	250	HPA	300	1800	TiN	90	TiN	90	26	1	10^7 at 2MV/cm, 33kHz[25]
Zr:HfO_2	12	50	TDMA-Hf	TEMA-Zr	H_2O	240	RTA	550	60	W/ TiN	40/20	TiN	40	41	1	N/A[49]
Zr:HfO_2	11.6	40	TDMA-Hf	TEMA-Zr	H_2O	300	None			TiN	10	InAs		22	1	10^6 at 3.5MV/cm, 10kHz[50]
Zr:HfO_2	10	50	TDMA-Hf	TEMA-Zr	N/A	200	FLA	630	5e-3	TiN	10	InAs		40	1	30000 at 3MV/cm, 100kHz[51]
Zr:HfO_2	15	40	TDMA-Hf	TEMA-Zr	H_2O	240	RTA	550	30	TiN	40	TiN	20	25	1.5	10^8 at 3MV/cm, 100kHz[52]
Zr:HfO_2	12	50	TDMA-Hf	TEMA-Zr	H_2O	200	RTA	370	N/A	TiN	14	InAs		42	1.2	N/A[53]
Zr:HfO_2	10	50	TEMA-Hf	TEMA-Zr	O_3	260	RTA	450	N/A	TiN	50	TiN	50	44	0.95	10^9 at 2.5MV/cm, 100kHz[64]
Zr:HfO_2	10	50	TEMA-Hf	TEMA-Zr	H_2O	240	RTA	400	TiN dep	TiN	15	TiN	15	20	1	10^{10} at 2.5MV/cm[54]
Zr:HfO_2	10	50	TEMA-Hf	TEMA-Zr	O_3	250	RTA	400	30	W	50	Pt/W	100/50	46	1.5	N/A[55]
Zr:HfO_2	2.5	50	TEMA-Hf	TEMA-Zr	O_3	250	RTA	400	30	W	50	Pt/W	100/50	28.4	1.5	N/A[55]
Zr:HfO_2	8.4	50	TEMA-Hf	TEMA-Zr	H_2O	300	RTA	400	30	TiN	25	TiN	25	46	1	N/A[56]
Zr:HfO_2	4	50	TEMA-Hf	TEMA-Zr	H_2O	300	RTA	500	30	TiN	25	TiN	25	23	1	3x10^{10} at 3MV/cm, 200kHz[56]
Zr:HfO_2	10	50	TEMA-Hf	TEMA-Zr	O_2 plasma	300	RTA	300	60	TiN	100	TiN	15	34	1	N/A[57]
Zr:HfO_2	10	57	TEMA-Hf	TEMA-Zr	H_2O	300	RTA	300	60	TiN	100	TiN	15	24	1	10^7 at 3MV/cm, 33kHz[58]
Zr:HfO_2	10	50	TEMA-Hf	CpZr	O_3	230	RTA	600	20	TiN	10	Si		52	N/A	N/A[38]
Zr:HfO_2	10	50	CpHf	CpZr	O_3	300	RTA	450	20	TiN	10	TiN	10	45	1	5x10^5 at 4MV/cm, 100kHz[59]
Zr:HfO_2	10	50	CpHf	CpZr	O_2 plasma	300	RTA	450	20	TiN	10	TiN	10	46	1	10^5 at 4MV/cm, 100kHz[59]
Zr:HfO_2	10	65	CpHf	CpZr	O_3	320	None			TiN	100	TiN	200	47.6	1.5	10^6 at 3.5MV/cm[60]
Zr:HfO_2	10	70	CpHf	CpZr	O_3	320	None			TiN	100	TiN	200	36	1.5	10^7 at 3.5MV/cm[61]
Zr:HfO_2	10	70	CpHf	CpZr	O_3	320	RTA	500	10	TiN	100	TiN	200	13	1	10^7 at 3.5MV/cm[61]
Zr:HfO_2	5	25	$HfCl_4$	$ZrCl_4$	H_2O	300	RTA	450	60	TiN	10	TiN	10	47	1	10^8 at 1.9MV/cm[62]
Zr:HfO_2	10	50	$HfCl_4$	$ZrCl_4$	H_2O	300	Furnace	300	7200	TiN	N/A	TiN	N/A	30	1	N/A[63]

[a]Deposition, [b]Temperature, [c]Top electrode, [d]Thickness, [e]Bottom electrode, [f]Not available.

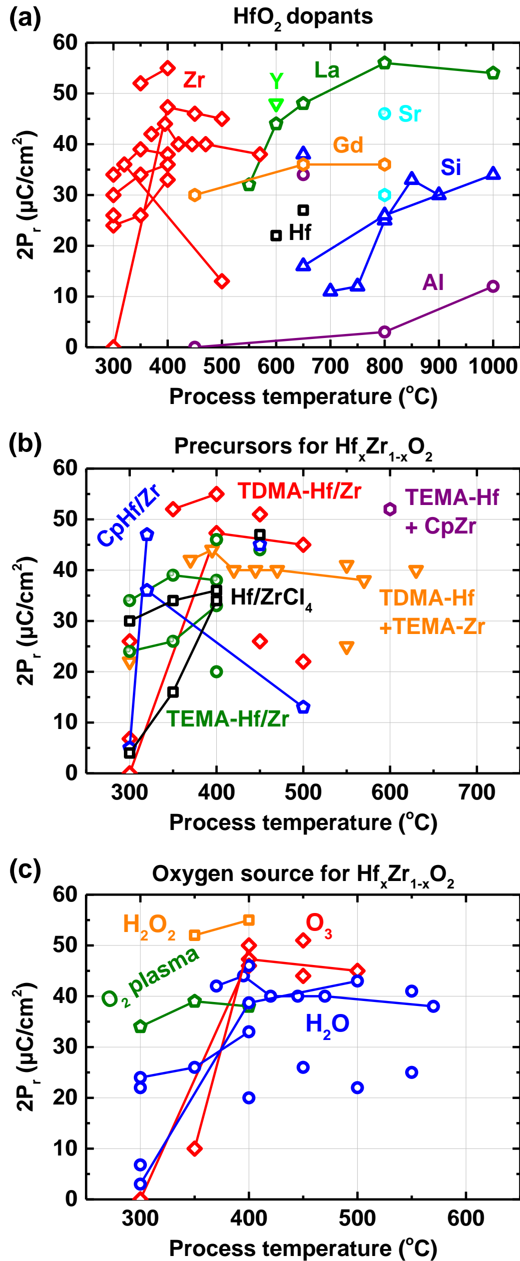

Figure 2. Summary of remnant polarization values as a function of process temperature of HfO_2-based ferroelectrics from previously reported data as shown in Table 1. The highest temperature step in the fabrication process, which includes annealing and deposition, was referred to as the process temperature. (a) Effect of dopants on ferroelectricity of HfO_2-based film.[25,29,37,38,41–48,53,57–59,61,63,69] (b) Effect of precursor selection in HZO films ferroelectricity.[25,29,38,49–64,66–69] (c) Oxygen source effect on the ferroelectric temperature of HZO films.[25,29,49–58,64,66–69]

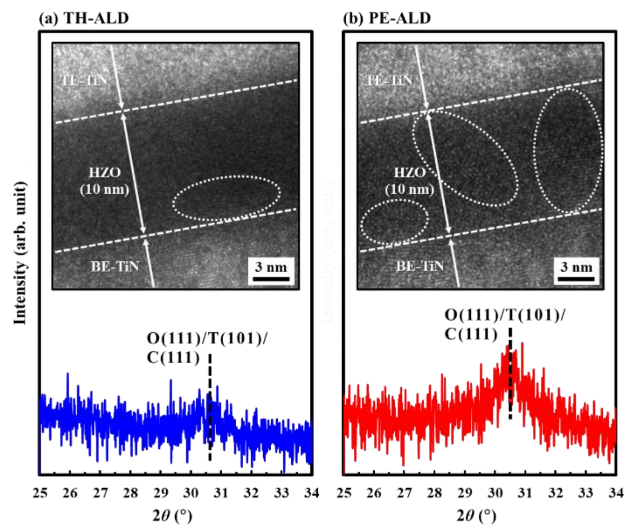

Figure 3. XRD patterns of as-grown HZO films deposited by (a) TALD and (b) PEALD at 300 °C. The insets show cross-sectional TEM images of MFM capacitors with as-grown (a) TALD and (a) PEALD HZO films. Reprinted with permission from ref 57 and 58. Copyright 2019 Elsevier and 2021 AIP Publishing, licensed under a Creative Commons Attribution (CC BY) license.

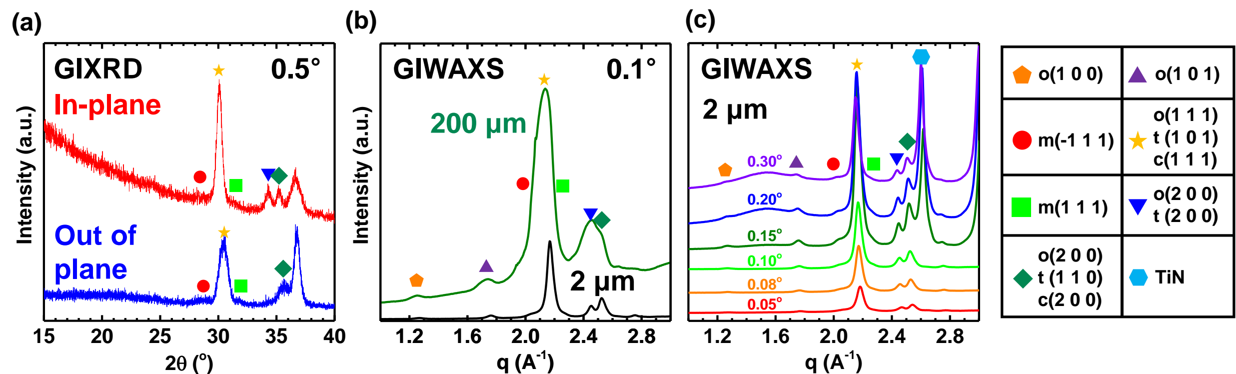

Figure 4. Phase analysis of ferroelectric 10 nm HZO film on TiN using Rigaku Smartlab XRD and National Synchrotron Light Source II at Brookhaven National Lab. The TE-TiN was removed before the measurements. (a) GIXRD in-plane and out-of-plan diffraction pattern with 0.5° incident angle measured with Rigaku Smartlab XRD. (b) GIWAXS measurements were performed by synchrotron light source at BNL with 0.1° incident angle using two different beam sizes. Smaller beam size shows lower intensity, but higher q resolution compared to bigger beam size. (c) Incidence angle dependence of GIWAXS spectra measured using 2 μm microbeam condition. Kim, J.-H. The University of Texas at Dallas, Richardson, TX, Unpublished data, 2023.

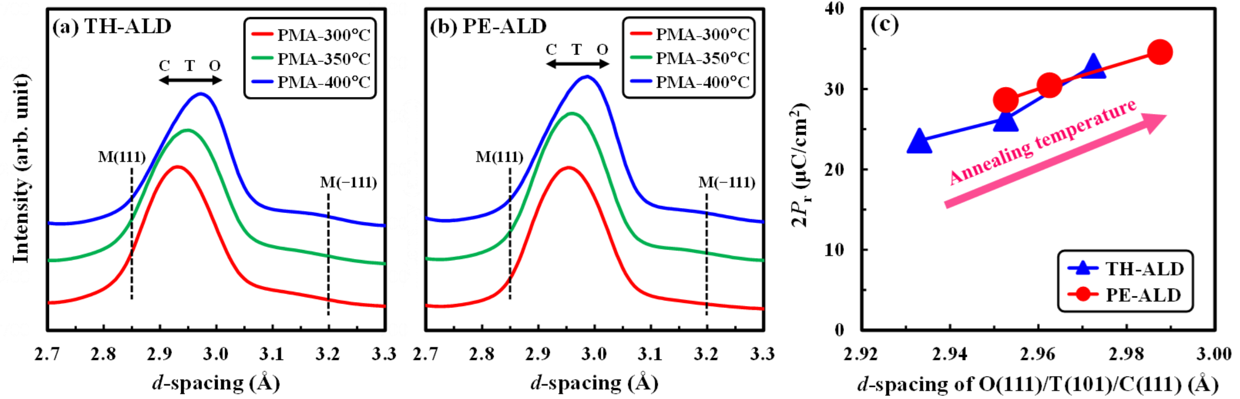

Figure 5. Synchrotron GIWAXS patterns of (a) TALD and (b) PEALD HZO films prepared via the PMA process at 300–400 °C. (c) Relationship between the *d*-spacing of O(111)/T(101)/C(111) phases, as extracted from the synchrotron GIWAXS patterns, and the $2P_r$ values of TALD and PEALD HZO films prepared via the PMA process at 300–400 °C. Reprinted with permission from ref 58. Copyright 2021 AIP Publishing, licensed under a Creative Commons Attribution (CC BY) license.

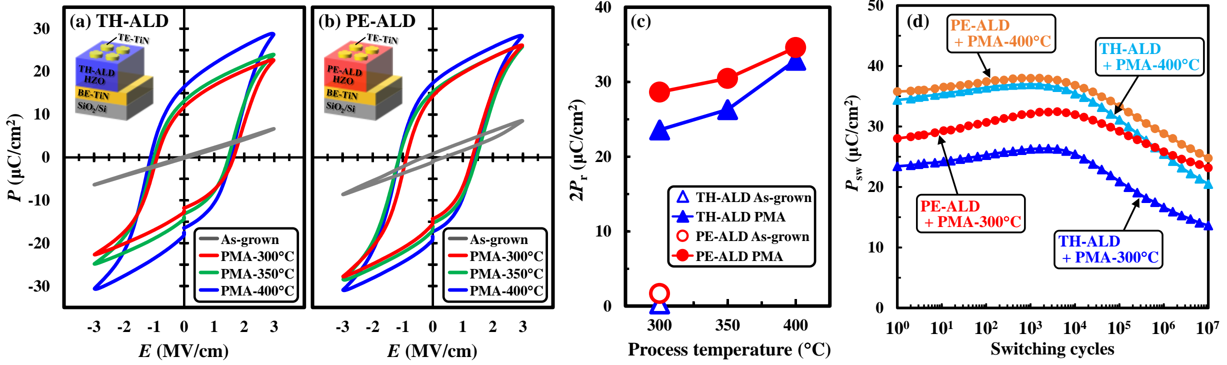

Figure 6. *P*–*E* hysteresis curves for MFM capacitors with 10-nm-thick (a) TALD and (b) PEALD HZO films. (c) Relationship between the process temperature and the $2P_r$ values extracted from the *P*–*E* hysteresis curves of the TALD and PEALD HZO films. (d) Endurance properties of MFM capacitors with TALD and PEALD HZO films after the PMA process at 300 and 400 °C. The PUND measurements were performed to evaluate the P_{sw} during field cycling. Reprinted with permission from ref 58. Copyright 2021 AIP Publishing, licensed under a Creative Commons Attribution (CC BY) license.

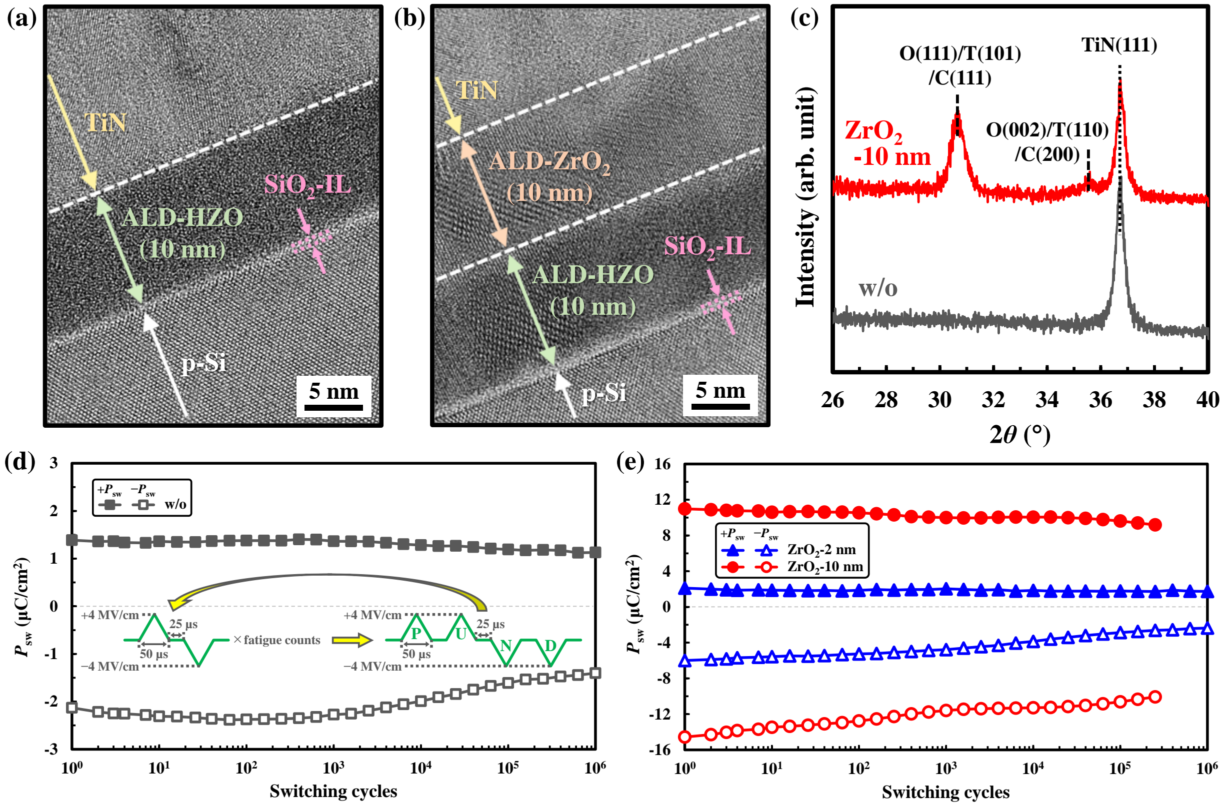

Figure 7. Cross-sectional TEM images of (a) w/o and (b) ZrO_2-10-nm MFS capacitors after the PMA process at 300 °C. (c) GIXRD patterns of the PMA-treated w/o and ZrO_2-10-nm MFS capacitors. Endurance properties of (d) a w/o MFS capacitor and (e) ZrO_2-2-nm and ZrO_2-10-nm MFS capacitors after the PMA process at 300 °C. Reprinted with permission from ref 121. Copyright 2022 AIP Publishing, licensed under a Creative Commons Attribution (CC BY) license.

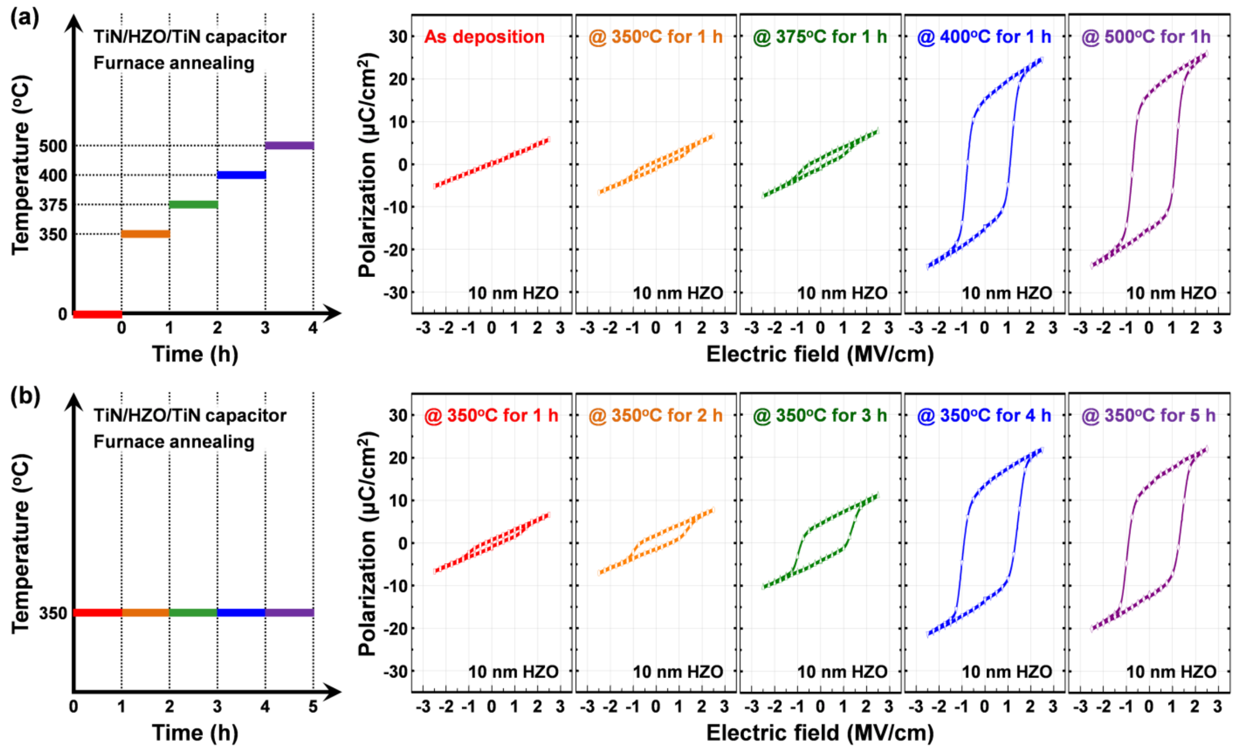

Figure 8. P-E hysteresis curves of TiN/HZO/TiN capacitors (a) annealed at 350-500°C for 1 hour and (b) annealed at 350°C for 1-5 hours. Reproduced with permission from ref 26. Copyright 2023 KIEEME.

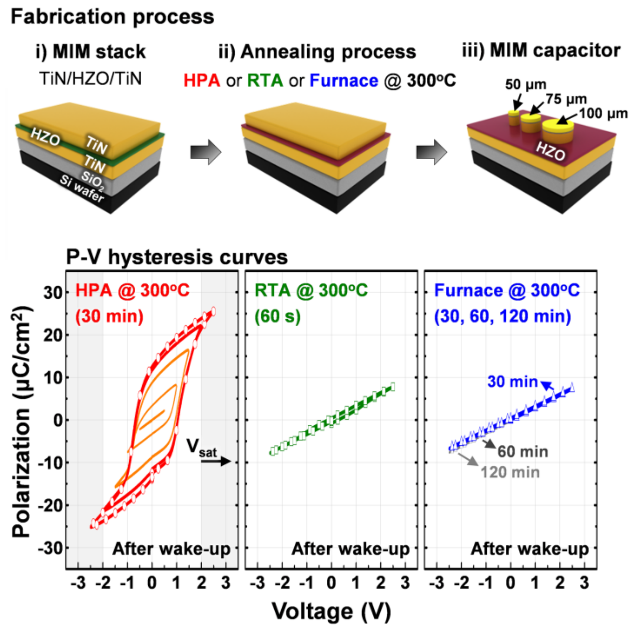

Figure 9. Schematic illustration of the fabrication process and P-V hysteresis curves of TiN/HZO/TiN capacitors annealed at 300°C using HPA, RTA, and furnace. Reproduced with permission from ref 25. Copyright 2021 AIP Publishing.

TABLE OF CONTENTS (TOC)

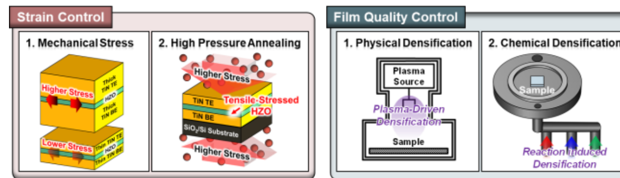

Schematic illustration of the various strategies to control film strain and density using stressors and ALD process to achieve low-temperature ferroelectric technology.